

Alternating Gradient Focusing and Deceleration of Polar Molecules

Hendrick L. Bethlem^{1,2,*}, M.R. Tarbutt³, Jochen Küpper¹, David Carty^{1†}, Kirstin Wohlfart¹, E.A. Hinds³, and Gerard Meijer¹

¹*Fritz-Haber-Institut der Max-Planck-Gesellschaft,
Faradayweg 4-6, D-14195 Berlin, Germany*

²*Laser Centre Vrije Universiteit, De Boelelaan 1081,
NL-1081HV Amsterdam, The Netherlands*

³*Centre for Cold Matter, Blackett Laboratory,
Imperial College London, SW7 2BW, United Kingdom*

(Dated: April 2, 2018)

Beams of polar molecules can be focused using an array of electrostatic lenses in alternating gradient (AG) configuration. They can also be accelerated or decelerated by applying an appropriate high voltage switching sequence to the lenses. AG focusing is applicable to molecules in both low-field and high-field-seeking states and is particularly well suited to the problem of decelerating heavy molecules and those in their ground rotational state. We describe the principles of AG deceleration and set out criteria to be followed in decelerator design, construction and operation. We calculate the longitudinal and transverse focusing properties of a decelerator, and exemplify this by 2D-imaging studies of a decelerated beam of metastable CO molecules.

PACS numbers: 33.80.Ps, 33.55.Be, 39.10.+j

I. INTRODUCTION

During the last few years, a variety of techniques have been demonstrated to produce samples of trapped neutral molecules [1]. One of these exploits the force that a polar molecule experiences in an inhomogeneous electric field to change its motion. This force attracts molecules to regions of high or low electric field depending on the sign of the Stark shift. Some small polar molecules in low-field seeking states have been decelerated using a series of pulsed electric fields. These include CO [2], NH₃ and ND₃ [3], OH [4, 5], NH [6], H₂CO [7] and SO₂ [8]. In the case of ND₃ [3] and OH [5] packets of Stark decelerated molecules have subsequently been electrostatically trapped. We aim to extend this deceleration method to heavy polar molecules including bio-molecules. Of particular interest are molecules such as YbF which are being used in experiments aimed at detecting time-reversal symmetry violating interactions leading to a permanent electric dipole moment (EDM) of the electron, which is a sensitive probe for physics beyond the Standard Model [9, 10]. Decelerated molecules offer an increased sensitivity for these experiments. Stark deceleration of bio-molecules allows one to prepare samples of selected conformers for further studies.

Deceleration of heavy polar molecules is difficult for two reasons: (i) For a given velocity of the beam, the kinetic energy of the molecules, and thus the number of electric field stages required to bring the molecules to a standstill, is proportional to their mass. (ii) At the

electric field strengths required for deceleration, all low-lying rotational levels of heavy molecules have a negative Stark shift. In these states the molecules are attracted to a maximum of the electric field, i.e. to the electrodes. In order to guide high-field-seeking molecules through the decelerator dynamic focusing schemes need to be used which, typically, have an order of magnitude smaller acceptance than the schemes used to guide low-field-seeking molecules. We have recently demonstrated a decelerator for high-field seeking molecules [11, 12] using the alternating gradient principle. Those experiments showed the feasibility of the AG deceleration technique, which we discuss in detail here.

Our paper is organized as follows. In Sec. II we outline the method of alternating gradient Stark deceleration, and set out some general principles that will guide us through the rest of the paper. In Sec. III the Stark shift of polar molecules is discussed in more detail, drawing on the particular cases of metastable CO, YbF and benzonitrile. In Sec. IV we present three simple electrode geometries that may be used to make a single lens of the alternating gradient array and discuss the merits of these geometries. In Sec. V we consider the motion of the molecules through the decelerator, present the trajectories and phase-space distributions, and calculate the transmission of both idealised and real decelerators. In Sec. VI we present an experimental study of the transverse focusing properties of an AG decelerator, by measuring the two-dimensional distributions of a decelerated beam of metastable CO molecules. Our results are compared to calculations. A summary of our main conclusions and a discussion of future prospects are given in Sec. VII.

[†]Present address: Physical and Theoretical Chemistry Laboratory, South Parks Road, Oxford OX1 3QZ, United Kingdom

*Electronic address: rick@fhi-berlin.mpg.de

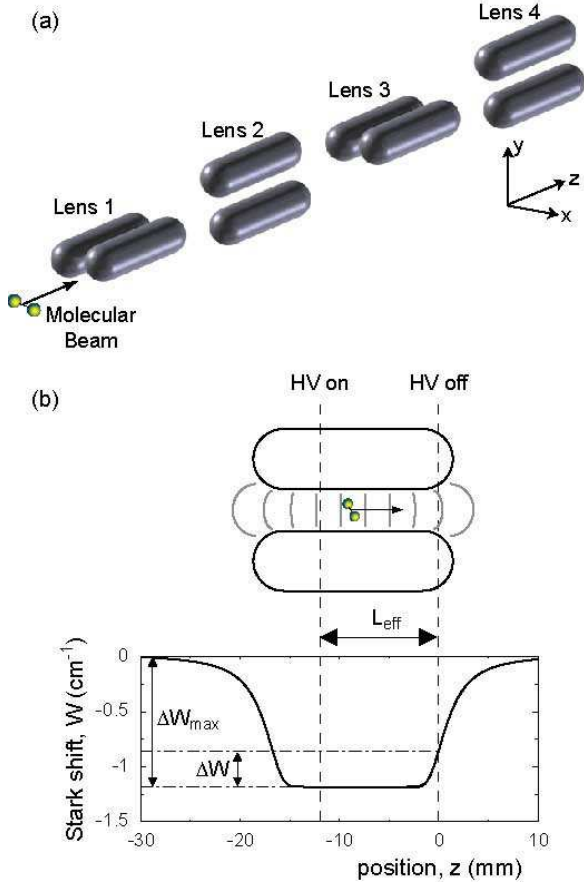


FIG. 1: (a) Layout of an alternating gradient decelerator for polar molecules showing the first four deceleration stages. Each electrode pair acts both to focus and decelerate the molecules. (b) Cross-section of a single lens formed from two 20 mm long rods with hemispherical ends, 6 mm in diameter and spaced 2 mm apart. Potential energy along the z -axis for metastable CO molecules in the $a^3\Pi$, $J=1$, $\Omega=1$, $M\Omega=+1$ level, when the potential difference between the electrodes is 20 kV. The high-voltage switching procedure is indicated: the voltages are turned on when the bunch of molecules reaches the ‘HV on’ position, and are turned off once they reach the ‘HV off’ position.

II. GENERAL PRINCIPLES

A Stark decelerator consists of a series of capacitor plates. A polar molecule that has its dipole oriented anti-parallel to the electric field (a low-field seeker) will gain potential energy when entering one of these capacitors and will therefore be decelerated. When leaving the field of the capacitor it will lose potential energy and so be accelerated back to its initial velocity. If we switch the field off before the molecule has left the capacitor, it will keep its lower velocity. Similarly, a molecule that has its dipole oriented parallel to the electric field (a high-field seeker) will accelerate when entering, and decelerate when leav-

ing one of these capacitors. Again, by switching the electric fields at the appropriate times the molecule will be decelerated. A series of switched electric fields can thus be used to decelerate a pulsed molecular beam. The initial velocity of a seeded supersonic beam of molecules is in the range 250–2000 m/s, depending on the mass and temperature of the carrier gas. Typically, more than 100 stages are required to decelerate these beams to zero velocity. In order to have useful transmission, it is therefore of utmost importance that the trajectories through the decelerator are stable.

For a force field, $\vec{F}(\vec{r})$, to keep a particle in static equilibrium around $\vec{r} = 0$, two conditions must be met. The applied force must vanish at $\vec{r} = 0$, and, for small displacements, the force field should tend to restore the particle towards $\vec{r} = 0$ [53]. To achieve the latter it is necessary that the divergence of the force be negative, $\vec{\nabla} \cdot \vec{F} < 0$ [54]. The force acting on the molecules in an inhomogeneous electric field is given by:

$$\vec{F}(\vec{r}) = -\vec{\nabla}W(E), \quad (1)$$

with $W(E)$ being the Stark shift of a polar molecule in an electric field of magnitude $E = |\vec{E}|$. The properties of this force field were analyzed in a seminal paper by Auerbach, Bromberg and Wharton [13]. For molecules that experience a linear Stark shift in the applied field, $W = -\mu_{eff}E$, it was shown that:

$$\vec{\nabla} \cdot \vec{F} = \frac{\mu_{eff}}{E^3} \sum_{i,j,k=1}^3 \left[\left(\frac{\partial \Phi}{\partial x_k} \right)^2 \left(\frac{\partial^2 \Phi}{\partial x_i \partial x_j} \right)^2 - \left(\frac{\partial \Phi}{\partial x_i} \right) \left(\frac{\partial \Phi}{\partial x_k} \right) \left(\frac{\partial^2 \Phi}{\partial x_i \partial x_j} \right) \left(\frac{\partial^2 \Phi}{\partial x_k \partial x_j} \right) \right], \quad (2)$$

where Φ is the electrostatic potential and μ_{eff} is an effective dipole moment which depends on the particular molecular state. Using Schwartz’s inequality, it can be seen that the sum is always positive. Therefore, for molecules having a linear Stark shift the sign of $\vec{\nabla} \cdot \vec{F}$ is determined solely by the sign of μ_{eff} [55]. Thus, for molecules that have a negative μ_{eff} (low-field seekers), $\vec{\nabla} \cdot \vec{F} \leq 0$, and focusing is straightforward. For molecules that have a positive μ_{eff} (high-field seekers), $\vec{\nabla} \cdot \vec{F} \geq 0$, and focusing is more problematic.

The difficulty of focusing high-field-seeking molecules is analogous to the situation for ions, for which $\vec{\nabla} \cdot \vec{F} = q\vec{\nabla} \cdot \vec{E} = 0$ in free space, where q is the charge of the ion. Therefore, techniques routinely applied to ions can be translated to polar molecules. Three schemes are generally employed. (i) *Circular motion*; In a cyclotron the curvature of the trajectory adds a force which, in an appropriately shaped magnetic or electric field, stabilizes the motion of the ions [14]. A similar stabilization can be achieved for polar molecules. For example, molecules

that have a linear Stark shift in an applied field flying at a distance r from the axis of a capacitor formed by two coaxial cylinders, experience a force proportional to $1/r^2$. They therefore move in stable Kepler-type orbits around the central electrode. This technique has been used to focus molecules in high-field seeking states [15–17]. (ii) *Alternating gradient (AG) focusing*; Alternating gradient focusing of charged particles was pioneered by Courant, Livingstone and Snyder [18, 19] and is now applied in virtually all particle accelerators. An AG array consists of a series of magnetic or electric quadrupole lenses that focus ions in one direction while defocusing them in the other direction. By alternating the orientation of these fields it is possible to obtain net focusing in both directions. As this stabilization is due to the motion of the ion itself, it is referred to as ‘dynamic’ stability. Application of the technique to focus polar molecules was demonstrated experimentally by Kakati and Lainé [20], by Günther et al. [21–23] and by Bromberg [24]. More recently, the AG technique was used to focus metastable argon atoms released from a magneto-optical trap [25] and cesium atoms in an atomic fountain [26]. Furthermore, the transmission of methylfluoride molecules through a 15 m long AG beamline was modelled and optimized [27]. (iii) *Einzel lens*; In an Einzel or uni-potential lens an ion is subjected to an acceleration along the axial direction followed by an equal deceleration. In the radial direction ions are focused on entering the fringe field and defocused on leaving it. This results in a net (dynamic) focusing effect. The focusing is only effective when the change in kinetic energy of the ions is a substantial fraction of their initial energy and so Einzel lenses are only useful for low energy ion beams. A similar effect is obtained for polar molecules entering and leaving a field region, but again its usefulness is restricted to very low energy beams, e.g. for loading slow molecules into a trap.

For a decelerator (or accelerator) for polar molecules alternating gradient focusing seems the obvious choice. Fig. 1(a) shows the general form of the experimental setup. The AG lenses are formed from a pair of cylindrical electrodes to which a voltage difference is applied. Molecules will be defocused in the plane containing the electrodes while being focused in the orthogonal plane. As the molecules move down the beamline the focusing and defocusing directions alternate. The defocusing lenses have a smaller effect on the molecules than the focusing lenses, not because their power is smaller (it is not), but because the molecules tend to be close to the axis when they are inside the defocusing lenses and further away from the axis when they encounter the focusing lenses. Molecules in high-field seeking states are accelerated while entering the field of an AG lens and are decelerated while leaving the field. By simply switching the lenses on and off at the appropriate times, AG focusing and deceleration of polar molecules can be achieved simultaneously. Fig. 1(b) shows the potential energy (the Stark shift) along the z -axis of a single lens for a representative high-field seeking molecule. The molecules enter

each lens with the electric fields turned off so that their speed is unchanged as they enter. The fields are then suddenly turned on, and the high-field seeking molecules are decelerated as they leave the lens and move from a region of high field to one of low field. This process is repeated until the molecules reach the desired speed. As indicated in the figure, the amount of deceleration can be controlled by choosing how far up the potential hill the bunch of molecules has climbed before the fields are turned off (i.e. by moving the ‘HV off’ point in Fig. 1(b)). Similarly, the effective length of each lens, L_{eff} , can be controlled by varying the amount of time that the fields are on (i.e. by moving the ‘HV on’ point in Fig. 1(b)).

A prototype machine of this type has been used to decelerate high-field seeking metastable CO molecules from 275 m/s to 260 m/s [11]. More recently, an improved device decelerated ground state YbF molecules from 287 m/s to 277 m/s, corresponding to a 7% reduction of the kinetic energy [12]. Since then, YbF and CaF molecules have been decelerated using an array of 21 lenses at Imperial College London, while at the Fritz-Haber-Institut in Berlin, CO and benzonitrile molecules have been decelerated using an array of 27 lenses. These results will be presented elsewhere.

III. THE STARK SHIFT IN POLAR MOLECULES

We now discuss the Stark shift in more detail for some representative polar molecules. The Stark shift of a molecule is a function of the electric field magnitude $E = |\vec{E}|$. It is useful to define a dimensionless parameter, λ , that describes the strength of the electric field. In the context of an idealized rigid-rotor molecule [28] with dipole moment μ and rotational constant B (in energy units), the appropriate dimensionless ratio is $\lambda = \mu E/B$. When the electric field is ‘weak’, $\lambda \ll 1$, the Stark shift is quadratic in λ and can be calculated using second order perturbation theory. The states are best labelled by the rotational angular momentum quantum number J , and its projection, M , onto the field axis. If λ is increased, states of different J are increasingly strongly mixed until, in the strong-field limit ($\lambda \gg 1$), the states are called ‘pendular’ [29–31]. In that case they are labelled by the quantum numbers v_p and M , with $v_p = 2J - |M|$, and states of the same v_p but different M are degenerate. In this strong-field limit, all the low-lying states are high-field seekers. This limit is of most interest for our present discussion. Within this high-field, pendular state model, the Stark shift, W , is given by

$$W(v_p, \lambda)/B = -\lambda + (v_p + 1)(2\lambda)^{1/2}, \quad (3)$$

showing that the Stark shift becomes asymptotically linear in the electric field.

We find it useful to define the effective dipole moment, μ_{eff} , more generally as

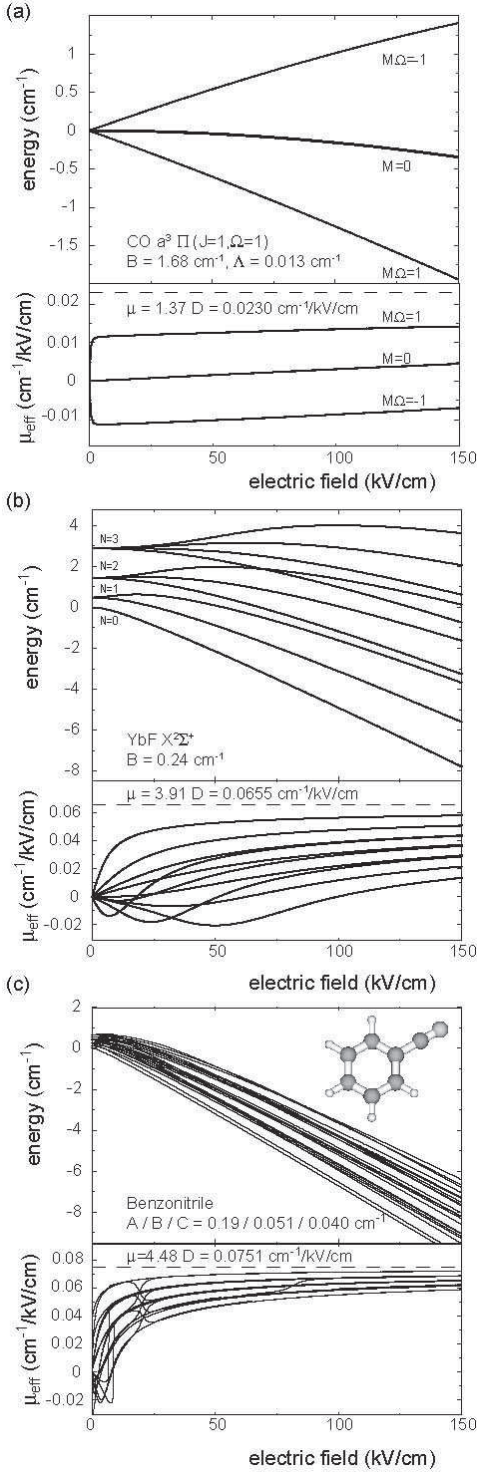


FIG. 2: Stark shifts and effective dipole moments for (a) the $J=1, \Omega=1$ levels of the $a^3\Pi$ state of CO, (b) the lowest four rotational levels in the ground state of YbF and (c) the lowest eight rotational levels of benzonitrile. In (a) and (b) the basis set includes all levels up to $J=10$, while in (c) all levels up to $J=30$ were included.

$$\mu_{\text{eff}}(E) = -\frac{\partial W}{\partial E}, \quad (4)$$

which converges with increasing electric field to its maximum value μ , reached when the body-fixed dipole moment is parallel to the external electric field. From Eq. (3) and (4) the effective dipole moment is given, in the strong-field limit, by

$$\mu_{\text{eff}} = \mu \left(1 - \frac{v_p + 1}{\sqrt{2\lambda}} \right). \quad (5)$$

Note that the effective dipole moments of states having the same values of v_p converge once the strong-field criterion ($\lambda \gg 1$) is met. By contrast, the convergence of all the μ_{eff} to a single value is a much slower one, scaling as $\lambda^{-1/2}$ and so requiring $\lambda^{1/2} \gg 1$ for low values of v_p . In strong fields the effective dipole moment varies little with applied field, and for small changes of the field it can be approximated as a constant. This is a very useful approximation in the context of an alternating gradient lens where the field is high and does not vary greatly across the aperture of the lens.

Figure 2(a) shows the Stark splitting and the effective dipole moments for the $J=1, \Omega=1$ level of the $a^3\Pi$ excited state of CO. The electronic ground state of CO has a small dipole moment (0.1 Debye) and rotational levels in this state only experience a second order Stark effect in realizable fields. By contrast, the metastable $a^3\Pi$ state of CO (lifetime 3.7 ms) has a dipole moment of 1.37 Debye (1 Debye is equivalent to 0.0168 cm⁻¹/kV/cm). Being a Π -state, all the rotational levels are doubly degenerate. As the separation of the nuclear motion and the electronic motion is not exact, this degeneracy is lifted and each rotational level is split in zero electric field into two levels with opposite parity. For the $J=1, \Omega=1$ level this Λ -doublet splitting is $\Lambda=394$ MHz. The two Λ -doublet levels are coupled by an electric field, leading to levels with a mixed parity that have non-zero space-fixed electric dipole moment. The Stark shift of the two Λ -doublet levels in a small static electric field of magnitude E is found by diagonalizing the energy within a single rotational manifold:

$$W(E) = \pm \sqrt{\left(\frac{\Lambda}{2}\right)^2 + \left(\mu E \frac{M\Omega}{J(J+1)}\right)^2} \mp \frac{\Lambda}{2}, \quad (6)$$

where J denotes the total angular momentum, while Ω and M are the projections of J onto the body fixed and space fixed axes, respectively. At higher electric fields, the Stark effect includes coupling to states of the same M but different J . Since low-lying states have many states of higher J above them, this coupling ultimately turns them all into high-field seekers. For example, the uppermost level in Fig. 2(a) is weak-field seeking, but at fields

above ~ 400 kV/cm it becomes high-field seeking. The effective dipole moments for the lowest rotational levels of CO are shown below the Stark-curves in Fig. 2(a). Calculation of the Stark shift in metastable CO is discussed in detail by Jongma et al. [32].

Figure 2(b) shows the energy and effective dipole moments of YbF in the $X^2\Sigma^+$ electronic ground state as a function of the electric field strength [33]. The states are labelled by the rotational quantum number N and its projection onto the electric field axis, M_N . This Stark effect is caused by the mixing of rotational levels. The ground rotational state is high-field seeking at all fields. Other states, such as the $N = 1, M_N = 0$ state are low-field seeking at small electric fields but become high-field seeking at larger field values. For the $N = 1, M_N = 0$ state, the turning point occurs at an electric field of $\sim 5B/\mu$, corresponding to only ~ 18 kV/cm for the heavy YbF molecule. For the fields in Fig. 2(b), the high-field condition $\lambda \gg 1$ is satisfied, and one sees that the μ_{eff} values converge for states of the same $v_p = 2J - |M|$, but different M . It is also evident in the figure that convergence of the effective dipole moments to the single value, μ , is very slow, as discussed earlier.

In Fig. 2(c) we show the Stark effect and effective dipole moments in the lowest rotational states of benzonitrile, calculated using experimentally determined constants [34]. Benzonitrile is an asymmetric top, and therefore levels with the same J are mixed by the electric field as well as those having $\Delta J = \pm 1$. As a molecule of this size has rather small rotational constants, all rotational levels become high-field seeking in relatively weak electric fields. The jumps between dipole moment curves in Fig. 2(c) are caused by avoided crossings. Details on the calculation of the Stark shifted energy levels in an asymmetric top molecule can be found elsewhere [35].

Table I gives the relevant properties for Stark deceleration for a selection of polar molecules. These properties are the Stark shift, effective dipole moment, rotational constants and mass. Values are given at a field of 100 kV/cm and are for molecules in the electronic and rovibronic ground state (with the exception of metastable CO). The number of electric field stages required to bring molecules with a certain initial velocity to rest depends on the ratio of their Stark shift to their mass. The focusing properties of molecules flying at a certain velocity depend on the ratio of their effective dipole moment to their mass. One can see from the table that these molecules, though widely different in mass, have similar ratios of effective dipole moment to mass, and of Stark shift to mass, and so will be focussed and decelerated similarly. The Stark shifts and effective dipole moments are generally dependent on the specific quantum state that the molecule is in. For many experiments one would like to decelerate molecules in a variety of quantum states simultaneously. This can be done when all the rotational states have the same dependence on electric field, as is more or less the case for the polyatomic aromatic molecules with small rotational constants listed in the table. For com-

plex molecules such as tryptophan, the decelerator offers the intriguing possibility of selecting a specific conformational isomer out of the various conformers known to co-exist in a supersonic beam [41], as the individual conformers have distinctly different values of μ_{eff} .

IV. ELECTRODE GEOMETRY

A. The field of an infinitely long lens

Although the electrodes of a decelerator are in short segments along the beam direction, the basic focusing properties are best elucidated by first considering the case of long electrodes. In this section we discuss how to design a set of electrodes that minimizes the aberrations of an AG lens. In an aberration-free lens, molecules experience a harmonic interaction potential in the transverse plane. As discussed in Sec. II, the potential will focus along one direction and defocus along the other. For molecules that experience a linear Stark shift the ideal form for the field strength is also harmonic; $E(x, y) = E_0 + \eta(x^2 - y^2)$. As we shall see, this field cannot be realized but it is possible to produce a field that is a good approximation to this ideal one. We follow a similar approach to that given in [27].

In a region devoid of charges the electric field can be derived from the electrostatic potential Φ as $\vec{E} = -\vec{\nabla}\Phi$, with $\nabla^2\Phi = 0$. In 2D, Φ may be represented by a multipole expansion as:

$$\Phi(x, y) = \Phi_0 \left[\sum_{n=1}^{\infty} \frac{a_n}{n} \left(\frac{r}{r_0} \right)^n \cos(n\theta) + \sum_{n=1}^{\infty} \frac{b_n}{n} \left(\frac{r}{r_0} \right)^n \sin(n\theta) \right]. \quad (7)$$

Here $r = \sqrt{x^2 + y^2}$ and $\theta = \tan^{-1}(\frac{y}{x})$ are the usual cylindrical coordinates. a_n and b_n are dimensionless constants. r_0 and Φ_0 are scaling factors that characterize the size of the electrode structure and the applied voltages, respectively. The electric field magnitude at the centre is given by $E_0 = (\Phi_0/r_0)\sqrt{a_1^2 + b_1^2}$. The $n = 1$ terms in Eq. (7) represent a constant electric field, while the $n = 2$ and $n = 3$ terms represent the familiar quadrupole and hexapole fields that have been used extensively to focus molecules in low-field seeking states [42].

Equation (7) represents the most general form of the electrostatic potential consistent with Laplace's equation. Now we choose the coefficients to be suitable for making a good lens. We require the magnitude of the electric field to be non-zero at the origin, and symmetric under reflection in the x - and y -axes. To achieve this, we make Φ symmetric under reflection in the x -axis and anti-symmetric under reflection in the y -axis by setting all $b_n = 0$ and retaining only the terms of odd n . Anticipating the result that high-order terms only introduce

Molecule	Rotational state	Stark shift	Effective dipole	Rotational constants	Mass (amu)
		(cm ⁻¹) at 100 kV/cm	(cm ⁻¹ /kV/cm) at 100 kV/cm	(cm ⁻¹) A / B / C	
CO (<i>a</i> ³ Π ₁) [32]	$ J = 1, M\Omega = -1\rangle$	-1.25	0.0135	- / 1.68 / -	28
CaF [36, 37]	$ J = 1/2, M\Omega = +1/4\rangle$	-3.43	0.0420	- / 0.34 / -	59
YbF [33]	$ J = 1/2, M\Omega = +1/4\rangle$	-4.91	0.0569	- / 0.24 / -	193
ND ₃ [38]	$ J = 1, MK = -1\rangle$	-1.27	0.0134	- / 5.14 / 3.12	20
pyridazine [39]	$ J_{K_a K_c} M\rangle = 0_{00}0\rangle$	-5.59	0.0624	0.21 / 0.20 / 0.10	80
benzonitrile [34]	$ J_{K_a K_c} M\rangle = 0_{00}0\rangle$	-6.71	0.0711	0.19 / 0.051 / 0.040	103
tryptophan [40]	I $ J_{K_a K_c} M\rangle = 0_{00}0\rangle$	-6.25	0.0646	0.041 / 0.013 / 0.012	216
	II	-4.72	0.0494	0.039 / 0.014 / 0.012	
	III	-1.71	0.0183	0.033 / 0.017 / 0.013	
	IV	-11.68	0.120	0.032 / 0.016 / 0.013	
	V	-12.28	0.126	0.043 / 0.011 / 0.0096	
	VI	-11.37	0.116	0.045 / 0.011 / 0.0095	

TABLE I: A selection of polar molecules with their relevant properties for AG focusing and deceleration.

undesirable non-linearities into the force we choose to retain only a_1 , a_3 and a_5 . Hence:

$$\Phi(x, y) = \Phi_0 \left(a_1 \frac{x}{r_0} + a_3 \frac{(x^3 - 3xy^2)}{3r_0^3} + a_5 \frac{(x^5 - 10x^3y^2 + 5xy^4)}{5r_0^5} \right). \quad (8)$$

From this potential, we obtain the electric field magnitude, $E(x, y) = \sqrt{\left(\frac{\partial \Phi}{\partial x}\right)^2 + \left(\frac{\partial \Phi}{\partial y}\right)^2}$. Throughout the region $r < r_0$ this can be expanded as a power series in a_3 and a_5 . For the case $a_5 \ll a_3 \ll a_1$ we obtain

$$E(x, y) = E_0 \left(1 + \frac{a_3}{a_1} \frac{(x^2 - y^2)}{r_0^2} + 2 \left(\left(\frac{a_3}{a_1} \right)^2 - 3 \frac{a_5}{a_1} \right) \frac{x^2 y^2}{r_0^4} + \frac{a_5}{a_1} \frac{(x^4 + y^4)}{r_0^4} + \dots \right). \quad (9)$$

The first two terms have the desired form and dominate the expansion. The other terms produce focusing aberrations. It might appear advantageous to set $a_5/a_1 = (a_3/a_1)^2/3$ so as to cancel the cross term. However, the best policy is to minimize a_5/a_1 [27] because the $x^4 + y^4$ term is also a damaging aberration.

To produce these fields we need to choose electrodes whose surfaces map onto the equipotentials. We are free to choose a_3/a_1 either positive or negative and will discuss both cases in turn. For example, Fig. 3(a) shows equipotentials for $a_3/a_1 = +1/7$ and $a_5 = 0$. The choice of a_3 is constrained by the condition $a_3 \ll a_1$ while remaining large enough to provide significant focusing. The

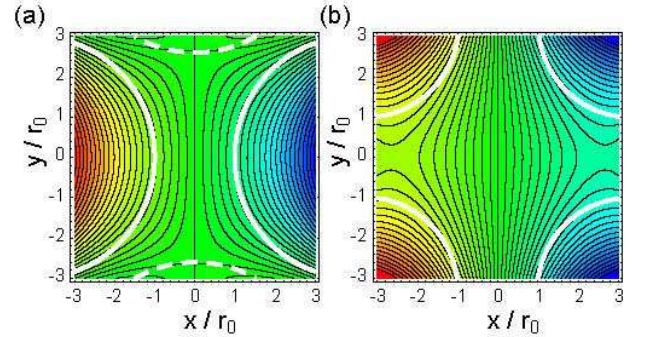


FIG. 3: Electrostatic equipotentials of equation (8) for the cases (a) $a_3/a_1 = +1/7$, $a_5 = 0$ and (b) $a_3/a_1 = -1/7$, $a_5 = 0$. Red and blue colourings correspond to positive and negative potentials respectively. The white lines show electrode surfaces designed to follow these contours.

solid white lines show electrodes, chosen to be circular for ease of construction, that match the equipotentials closely. They have radii of $R = 3r_0$ and are centred at $x = \pm 4r_0$, leaving a gap of $2r_0$. Because these electrodes do not match the equipotential exactly, higher order terms appear in the field. From a fit to the numerically calculated electrostatic potential we find for this geometry $a_3/a_1 = 0.143$ and $a_5/a_3 = 0.143$. It is noted that this two-rod field can be solved analytically and that $a_3/a_1 = (r_0/R) / (2 + r_0/R)$ and $a_5/a_3 = a_3/a_1$, in agreement with our fit.

The two charged rods are schematically depicted in Fig. 4(a), while Fig. 4(b) shows the magnitude of the electric field they produce as a function of distance along the x -axis (solid line) and y -axis (dashed line). A high-

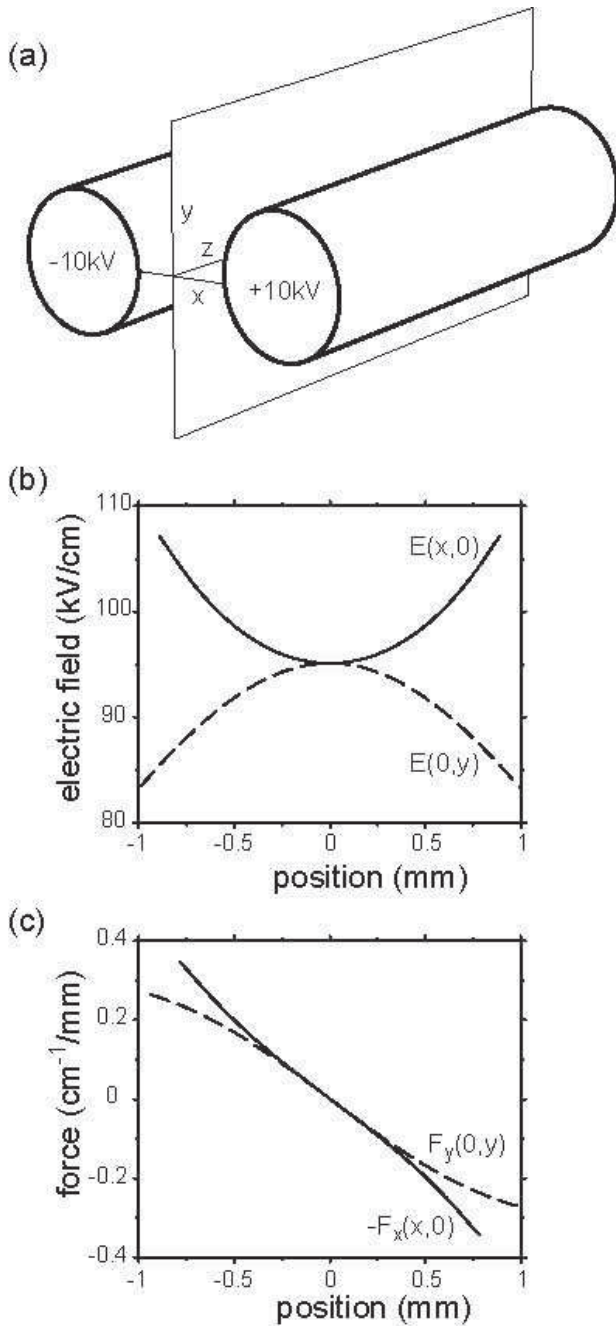


FIG. 4: The case of a two-rod lens. (a) Schematic view of the lens formed by two 6 mm diameter rods spaced 2 mm apart with a potential difference of 20 kV. (b) The electric field strength versus displacement along the x -axis (solid line) and the y -axis (dashed line). (c) Forces on a CO molecule in the high-field-seeking component of the $a^3\Pi$, $J=1$, $\Omega=1$ level. Dashed line: focusing force, $F_y(0,y)$. Solid line: defocusing force $F_x(x,0)$. The sign of this force has been reversed for ease of comparison. The gradient of both lines near the origin is $k=0.37 \text{ cm}^{-1}/\text{mm}^2$.

field seeker will be defocussed along x and focussed along y . Fig. 4(c) shows the corresponding forces exerted on CO molecules in the high field seeking component of the $a^3\Pi$, $J=1$, $\Omega=1$ level. The dashed line is the restoring force generated by a displacement along y , and is seen to be roughly linear. The solid line indicates the defocusing force along x . The sign of this force has been reversed so that the two can be compared directly. The two have equal gradients near the origin. Further away from the origin, the non-linearity due to a_5 acts to strengthen the defocusing power whereas the focusing is weakened. We will see later that this difference reduces the acceptance of an alternating gradient decelerator.

The rather large value of a_5/a_3 in this two-rod case can be reduced by adding two grounded electrodes tangential to the $\Phi = 0$ equipotentials at $y = \pm 2.65r_0$. These are shown dashed in Fig. 3(a), where for simplicity we have given the new rods the same radius R . In this case the coefficients become $a_3/a_1 = 0.157$ and $a_5/a_3 = 0.070$. At the expense of a slightly less ideal field one can position the four identical electrodes at the corners of a square. This has the advantage that one is free to choose in which plane the field focuses or defocuses by simply switching the voltages [43]. Using electrodes of radius r_0 with their centers placed on the corner of a square of side $3r_0$ yields $a_3/a_1 = 0.59$ and $a_5/a_3 = 0.056$. The rather large value of a_3/a_1 introduces higher order terms in the field, even though a_5/a_3 is quite small. A disadvantage of this field geometry is that the electric field strength on the beam axis is only half that on the electrodes. This makes the configuration less suited for use in a decelerator as the energy removed per stage is proportional to the central field. The geometry is useful for guiding molecules, as was recently demonstrated by Junglen et al. [44].

We turn now to the case of negative a_3/a_1 illustrated in Fig. 3(b) where we have chosen $a_3/a_1 = -1/7$ and $a_5 = 0$. This is well approximated by electrodes of radius $R = 2.3r_0$, with a minimum gap of $2r_0$ as shown by the solid white lines of Fig. 3(b). The precise field produced by these electrodes has $a_3/a_1 = -0.139$ and $a_5/a_3 = -0.014$. This geometry compares very favourably to the cases considered in Fig. 3(a) with regard to minimizing a_5 and hence the lens aberrations. As this geometry is symmetric, we can again reverse the focus and defocus directions very easily by interchanging the potentials on the top-right and bottom-left electrodes of Fig. 3(b). The field at the centre is 41% of the maximum, which is disadvantageous for a decelerator. This geometry was discussed by Lübbert et al. [23] in the context of focusing ICI molecules.

B. End effects

Until now we have assumed the electrodes to be infinitely long. We now discuss the influence of end effects. Eq. (2) gives the divergence of the force on a molecule with linear Stark shift. If we restrict our attention to the

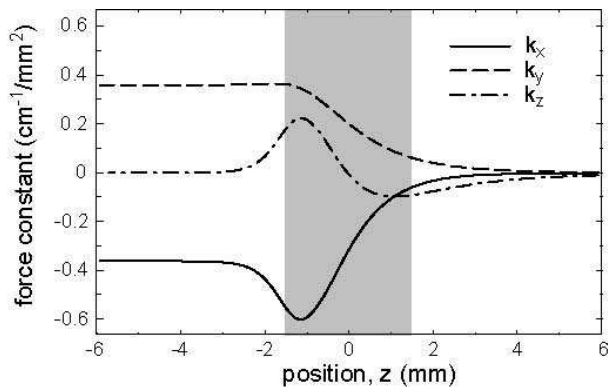


FIG. 5: The ‘force constants’ for CO ($a^3\Pi$, $J=1$, $\Omega=1$, $M\Omega=+1$) along the molecular beam axis and near the exit of the lens shown in Fig. 1(b) and Fig. 4(a). Solid line: defocussing constant $k_x = -\partial F_x/\partial x$. Dashed line: focussing constant $k_y = -\partial F_y/\partial y$. Dash-dotted line: axial gradient $k_z = -\partial F_z/\partial z$. The three are linked by Eq. (10). The gray shaded area indicates the region of the lens’s hemispherical end.

axis of our beamline, this equation is greatly simplified. Consider, for example, the pair of electrodes shown in Fig. 4. The electrostatic potential is symmetric about the x - z -plane and the y - z -plane is one of antisymmetry with $\Phi = 0$ everywhere on this plane. All the electrode geometries considered here have this property. On the beamline, the intersection of these two planes, it follows that all the derivatives in equation (2) are zero apart from $\partial\Phi/\partial x$ and $\partial^2\Phi/\partial z\partial x$. Since $-\partial\Phi/\partial x$ is the only non-zero electric field component, its magnitude is the total electric field strength E . Thus, on axis,

$$\vec{\nabla} \cdot \vec{F} = \frac{\mu_{\text{eff}}}{E} \left(\frac{\partial E}{\partial z} \right)^2. \quad (10)$$

Inside the lens $\partial E/\partial z = 0$ and $\partial F_z/\partial z = 0$ and it follows that the spring constants in the two transverse directions $k_x = -\partial F_x/\partial x$, $k_y = -\partial F_y/\partial y$ are equal and opposite, as shown in Fig. 4(c). The equality $k_x = -k_y$ means that the focusing and defocusing powers are equal. In the fringe field of the lens $\partial E/\partial z \neq 0$ and $\partial F_z/\partial z \neq 0$ and we find that

$$\begin{aligned} k_x + k_y &= -\mu_{\text{eff}} \left(\frac{1}{E} \left(\frac{\partial E}{\partial z} \right)^2 - \frac{\partial^2 E}{\partial z^2} \right) \\ &= \mu_{\text{eff}} E \frac{\partial}{\partial z} \left(\frac{1}{E} \frac{\partial E}{\partial z} \right). \end{aligned} \quad (11)$$

Due to the inhomogeneity of the electric field along z , the defocusing force becomes larger than the focusing force near the exit of the lens, whereas the focusing force is larger than the defocusing force further away from the lens. This is illustrated in Fig. 5, that shows the three

force constants k_x , k_y and k_z for the high-field seeking CO molecules as they approach the end of a lens formed by two rods with hemispherical ends. In this figure, the origin of z is at the point of inflection ($\partial^2 E/\partial z^2=0$) and the region of the hemispherical ends is indicated by the grey shaded area. We begin with the left hand side of the figure where the end-effects are negligible. Here, $k_z = 0$ and therefore $k_x = -k_y = 0.37 \text{ cm}^{-1}/\text{mm}^2$ the same as in Fig. 4. As the molecules approach the exit of the lens, they experience a decelerating force which can be seen in the figure as a positive k_z . According to Eq. (10), this is accompanied by a corresponding decrease in the sum $k_x + k_y$. We see this as a strengthening of the defocusing constant k_x near the exit, which becomes nearly twice as strong as the focusing constant. As we will see in Sec. V A, this is another mechanism, in addition to the aberrations discussed in Sec. IV A, that significantly reduces the transmission of an AG decelerator. A more gradual termination of the rods, e.g. a prolate spheroid replacing the hemisphere, reduces both the first and second derivatives of E with respect to z and so reduces end-effects in accordance with Eq. (11). In comparison with the two-rod configuration, the four-rod arrangement of Fig. 3(b) is also found to have a more favourable field at the exit of the lens.

V. MOTION OF THE MOLECULES THROUGH THE DECELERATOR

In this section we investigate the motion of molecules through the decelerator and discuss criteria for optimizing the transmission. The first part of this section deals with transverse stability, and the second part with longitudinal stability. This division is based on the assumption that the transverse and longitudinal motions can be treated independently. This is an approximation whose validity we discuss at the end of the section.

A. Transverse motion

In describing the transverse motion, we start by assuming that the molecules experience a linear force that focuses them along one direction and defocuses them along the other. The orientation of successive lenses alternates. The lenses have lengths L and are separated by drift regions of length S where the molecules experience no force. For molecules moving with a constant velocity, v_z , along the molecular beam axis, the equation of motion in a lens can be written as $\partial^2 x/\partial z^2 \pm \kappa^2 x = 0$, where the plus sign applies in a focusing lens, and the minus sign applies in a defocusing lens. The number of oscillations per unit length inside a focusing lens is $\kappa/2\pi$ and is related to the force constant k by $\kappa = \sqrt{|k|/mv_z^2}$. We also define the angular oscillation frequency Ω which, for the linear Stark effect reads

$$\Omega = \sqrt{\frac{|k|}{m}} = \sqrt{\frac{\mu_{eff}}{m} \frac{2E_0 a_3}{r_0^2}}. \quad (12)$$

For a molecule with initial position $x(z_0)$ and velocity $v(z_0)$, the equation of motion can be written as

$$\begin{pmatrix} x(z) \\ v_x(z) \end{pmatrix} = M(z|z_0) \begin{pmatrix} x(z_0) \\ v_x(z_0) \end{pmatrix}. \quad (13)$$

The transfer matrix $M(z|z_0)$ is then given by

$$M(z|z_0) = \begin{cases} \begin{pmatrix} \cos \kappa l & \frac{1}{\Omega} \sin \kappa l \\ -\Omega \sin \kappa l & \cos \kappa l \end{pmatrix} & F: \text{focusing lens} \\ \begin{pmatrix} 1 & l/v_z \\ 0 & 1 \end{pmatrix} & O: \text{drift space} \\ \begin{pmatrix} \cosh \kappa l & \frac{1}{\Omega} \sinh \kappa l \\ \Omega \sinh \kappa l & \cosh \kappa l \end{pmatrix} & D: \text{defocusing lens} \end{cases} \quad (14)$$

where $l = z - z_0$. The transfer matrix is written as F in a focusing lens, as D in a defocusing lens and as O in a drift region.

The transfer matrix for any interval made up of subintervals is just the product of the transfer matrices of the subintervals:

$$M(z_2|z_0) = M(z_2|z_1)M(z_1|z_0). \quad (15)$$

A single repeating unit of the alternating gradient array has the transfer matrix $F(L).O(S).D(L).O(S)$. We have written the lengths L and S explicitly here, but will usually drop them. The transfer matrix for an array of N such units is $M = (FODO)^N$. Alternatively, it can be useful to introduce frequent deceleration sections into longer lenses using a configuration $M = (FO)^n(DO)^n$. This structure with $n = 3$ is used in the decelerator that we present in Sec. VI. In order for molecules to have stable trajectories through any such array it is necessary that all the elements of the transfer matrix remain bounded when N increases indefinitely. This is the case when $-1 < \frac{1}{2}Tr(M) < +1$ (see, for example, [45]).

It is useful to parameterize the transfer matrix of one repetitive unit with length l_{cell} as [19]

$$M(z + l_{cell}|z) = \begin{pmatrix} \cos \Phi + \alpha \sin \Phi & \beta \sin \Phi \\ -\gamma \sin \Phi & \cos \Phi - \alpha \sin \Phi \end{pmatrix} \quad (16)$$

where $\alpha(z)$, $\beta(z)$ and $\gamma(z)$ are z -dependent parameters with periodicity equal to that of the lattice and are known as the Courant-Snyder parameters. Φ is known as the phase-advance per cell. Note that $\beta(z)$ and $\gamma(z)$ are expressed in seconds and 1/seconds, respectively, rather than in meters and 1/meters as is customary in the charged particle accelerator literature. This follows

from our use of (x, v_x) as state variables, rather than $(x, v_x/v_z)$.

The Courant-Snyder parameters and the phase advance are related to one another:

$$\alpha(z) = -\frac{v_z}{2} \frac{d\beta(z)}{dz}, \quad (17a)$$

$$\gamma(z) = \frac{1 + \alpha^2(z)}{\beta(z)}, \quad (17b)$$

$$\Phi = \frac{1}{v_z} \int_z^{z+l_{cell}} \frac{1}{\beta(z')} dz'. \quad (17c)$$

Equation (17b) ensures that the matrix has unity determinant. When expressed in this form, the transfer matrix acquires an extremely useful property, namely that the matrix describing N lattice units is identical to the matrix for a single unit, but with Φ replaced by $N\Phi$. Equation (17c) shows that Φ is independent of z , since the integral is taken over one complete period of the periodic function β . Note that the stability criterion becomes $-1 < \cos \Phi < +1$ and so is satisfied if Φ is real.

The trajectory of a molecule moving through the ideal lattice is given by

$$x(z) = \sqrt{\beta(z)\epsilon_i} \cos(\phi(z) + \delta_i), \quad (18)$$

where ϵ_i and δ_i define the initial conditions of this particular molecule, and $\phi(z)$ is a z -dependent phase given by $\phi(z) = 1/v_z \int_0^z 1/\beta(z') dz'$. Equation (18) shows that the motion is a product of two periodic functions, the first of wavelength l_{cell} and the second of wavelength $2\pi l_{cell}/\Phi$. When $\Phi \ll 2\pi$, the first motion has a short wavelength and is known as the micromotion, while the second has a much longer wavelength and is called the macromotion. This motion is identical to that of an ion in an rf trap [46]. From $x(z)$ and the relationships that hold between the Courant-Snyder parameters, it can be shown that

$$\gamma(z)x^2 + 2\alpha(z)xv_x + \beta(z)v_x^2 = \epsilon_i. \quad (19)$$

This equation defines an ellipse in the phase-space whose coordinates are x and v_x . The shape of the ellipse evolves periodically with z , but always has the same area $\pi\epsilon_i$. A set of molecules having many different values of δ_i but the same value of ϵ_i will all lie on the same ellipse. Furthermore, a distribution of molecules with all possible values of δ_i and all values of ϵ_i in the range $0 < \epsilon_i < \epsilon$, will all lie inside the ellipse characterized by ϵ . Again, the shape of this ellipse evolves periodically, but its area is a constant, $\pi\epsilon$. The value of ϵ defines the size of the beam in phase-space, and is called the emittance of the beam. Equation (18) tells us that the transverse displacements of a set of molecules lie within a beam envelope given by

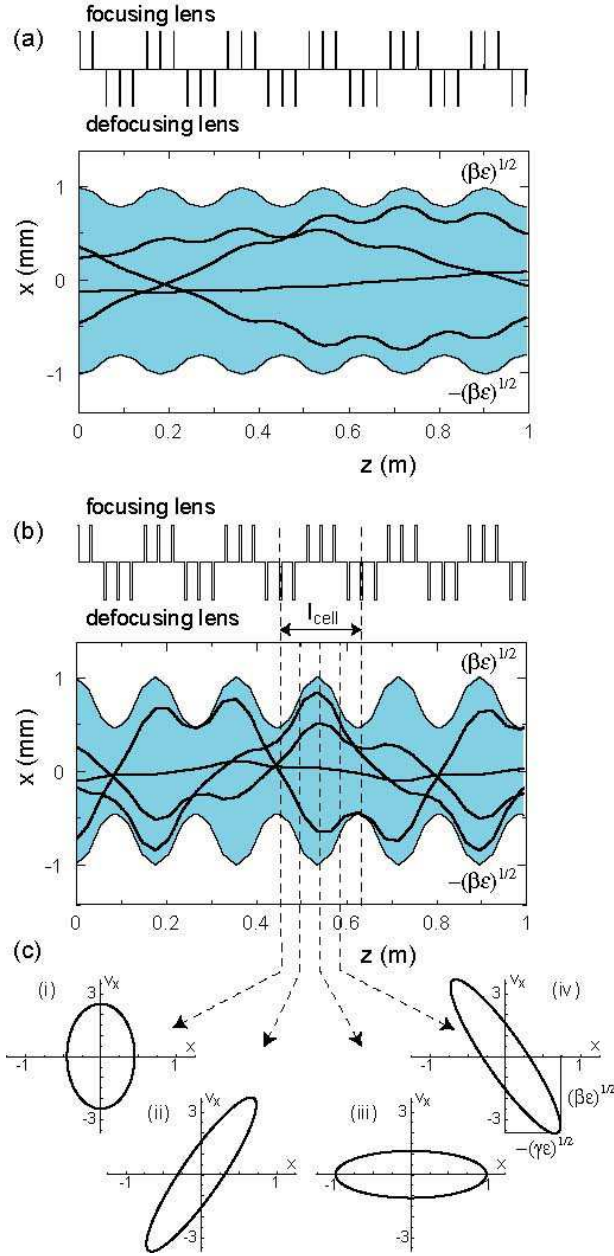


FIG. 6: (a) Trajectories of metastable CO molecules flying with a forward speed of 315 m/s through a $(FO)^3(DO)^3$ array. The parameters are $\kappa=38.7\text{ m}^{-1}$, $L=2\text{ mm}$ and $S=28\text{ mm}$, corresponding to $\Phi = \pi/6$. The shaded area shows the beam envelope bounded by $\pm\sqrt{\beta\epsilon}$, for a constant aperture of $d=2\text{ mm}$. (b) As (a), but with $L=6\text{ mm}$ and $S=24\text{ mm}$ corresponding to $\Phi = \pi/2$. (c) Phase-space area occupied by the beam at four positions in the unit cell with the position spread in mm and the velocity in m/s. (i) Centre of the defocusing set, (ii) between the defocusing and focusing sets, (iii) centre of the focusing set and (iv) between the focusing and defocusing sets.

the periodic function $\pm\sqrt{\beta(z)\epsilon}$. The velocity spread lies within a beam envelope given by $\pm\sqrt{\gamma(z)\epsilon}$.

In Fig. 6(a), some trajectories are plotted for metastable CO molecules travelling at 315 m/s through an alternating gradient array of type $(FO)^3(DO)^3$. The parameters of the array are $\kappa = 38.7\text{ m}^{-1}$, $L = 2\text{ mm}$ and $S = 28\text{ mm}$. Here, the phase-advance is $\pi/6$, and the micromotion of wavelength l_{cell} is superimposed on a macromotion whose wavelength is $12l_{\text{cell}}$. The shaded area of the figure shows the envelope of the transmitted molecular beam as it passes through the array. For such small values of the phase-advance, there is only a small difference between the maximum and minimum sizes of the beam envelope. As the phase-advance increases, the modulation of the beam envelope increases. This is demonstrated in Fig. 6(b) which shows trajectories and beam envelope for the same value of κ but with L increased to 6 mm and S decreased to 24 mm. The phase advance is now $\pi/2$, meaning that molecules return to their starting point after $4l_{\text{cell}}$. Figure 6(c) shows the phase-space distribution of the beam at four positions within the unit cell. In graph (i), the molecules are at the centre of the defocusing triplet. Here, the transverse size of the beam is at its minimum. The beam is diverging as it enters the focusing lenses (ii), and reaches its maximum size at the centre of the focusing triplet (iii). Graph (iv) shows that the beam is converging when it enters the defocusing lenses. The fact that the transverse size of the beam is larger in the focusing lenses than in the defocusing lenses, and that the forces are proportional to the off-axis displacements, accounts for the stability of the array. Since the stability relies upon the motion itself, it is commonly referred to as ‘dynamic’ stability.

We now calculate the transverse acceptance of the AG array. If we suppose that the array of lenses has a uniform aperture d throughout its length, then the beam whose emittance is ϵ will be transmitted without loss provided that the envelope fits inside the aperture, i.e. provided that $\sqrt{\beta(z)\epsilon} < d/2$ everywhere in the array. The transverse acceptance is the phase-space area occupied by the beam of largest emittance consistent with this criterion. This area is $\pi d^2/(4\beta_{\text{max}})$. From Fig. 6 we see that β is always a maximum at the centre of a focusing lens. To calculate the transverse acceptance of a lattice, we simply find the value of β at this position using Eq. (16) with $M = F(L/2) \cdot O(S) \cdot D(L) \cdot O(S) \cdot F(L/2)$. From this we find that β is a dimensionless number divided by Ω and so the acceptance is a multiple of $d^2\Omega$. d and Ω are the natural scaling parameters of the problem, and trajectories are invariant when plotted in $(x/d, v_x/(d\Omega))$ space.

In Fig. 7(a) and Fig. 7(b) we show the transverse acceptance calculated for lattices of $FODO$ and $(FO)^3(DO)^3$ cells, respectively. The acceptance is plotted as a function of the two dimensionless parameters that define the lattice, κL and κS . The acceptance (in either transverse direction) is given in units of $d^2\Omega$. One sees that the highest transverse acceptance is $0.186d^2\Omega$ and is obtained

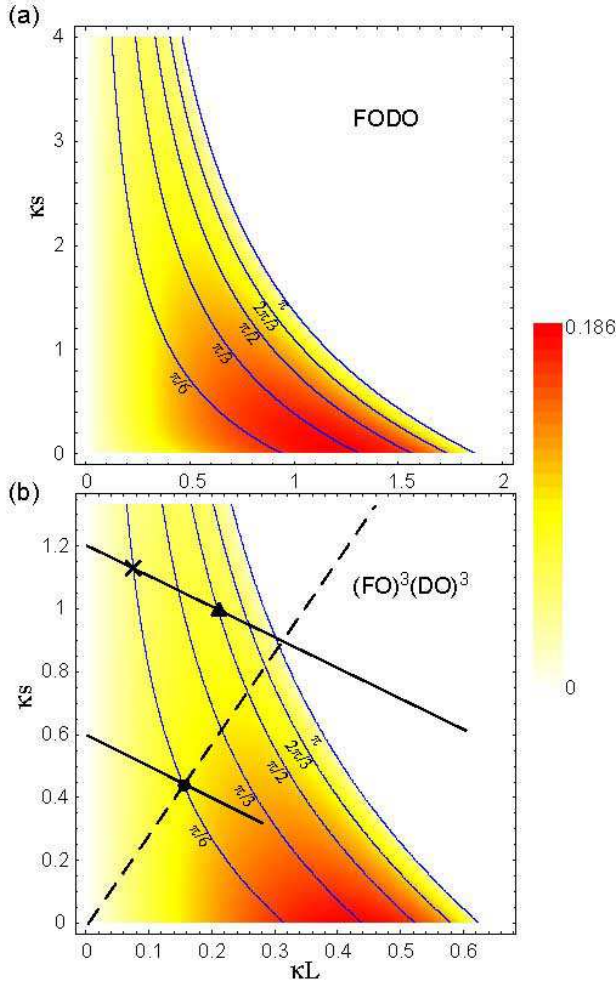


FIG. 7: Acceptance in one transverse direction of an infinitely long alternating gradient array, as a function of κL and κS . The acceptance is in units of $d^2\Omega$. Also shown are some contours of Φ which define the stability region. (a) A *FODO* array. (b) A $(FO)^3(DO)^3$ array. Straight solid and dashed lines, cross, triangle and dot are all referred to in the text.

when $\kappa L \sim 1$ and $S \ll L$. By contrast, a single, infinitely long focusing lens has an acceptance of $(\pi/4)d^2\Omega$, which is over four times larger. The figure also shows some contours of Φ , filling the region of stability bounded by the $\cos \Phi = \pm 1$ contours. The $\cos \Phi = +1$ contour corresponds to the vertical line $\kappa L = 0$.

In the experiments discussed in Sec. VI, the physical structure is fixed at $L + S = 30$ mm, but the effective length of the lenses can be varied by adjusting the high-voltage switch-on time (see Fig. 1(b)). Thus, the possible operating conditions lie on a straight line. Two such lines are shown in Fig. 7(b), indicating the operating conditions for the experiments where metastable CO was used at forward speeds of 630 m/s and 315 m/s. The cross and triangle placed on Fig. 7(b) correspond to the settings used to calculate the trajectories in Fig. 6(a) and

Fig. 6(b), with small and large phase advance respectively.

It is worth considering the scaling behaviour of the transverse acceptance with aperture, d . The acceptance along each direction scales as $d^2\Omega$, and Ω scales as $E_0^{1/2}d^{-1}$ (Eq. (12)). It is natural to operate the decelerator at the maximum field that can be achieved, which is determined by the breakdown field. If the transverse scale of the lenses is increased, with E_0 held constant by corresponding increases in the applied voltages, the acceptance along each direction is linear in d , implying that one should make the aperture as large as possible. There is, however, a practical upper bound V_{max} on the applied voltages. Once this value of V_{max} is reached, E_0 scales as d^{-1} and the acceptance in each transverse direction is proportional to $d^{1/2}$. Although the acceptance continues to increase with d , the decreasing value of E_0 results in an undesirable decrease in the energy loss per deceleration stage. Furthermore, increases in the acceptance cease to be useful once the transverse emittance of the beam is fully contained within the transverse acceptance of the decelerator.

We have seen that transverse stability depends on maintaining coherence between the oscillation of the molecules and the structure of the array. This makes the alternating gradient focussing particularly sensitive to deviations from the ideal, such as nonlinear terms in the force, end effects, and misalignments of the lens array. We now discuss the impact of each of these on the transverse acceptance. Fig. 8 shows the two-dimensional transverse acceptance of an $(FO)^3(DO)^3$ array calculated for the various lens geometries discussed in Sec. IV. The lens-lens spacing, $L + S$, is fixed at 30 mm, and the operating conditions correspond, for metastable CO, to the two straight, solid lines drawn on Fig. 7(b). Figure 8(a) is calculated for CO molecules with a forward speed of 315 m/s, while Fig. 8(b) is for a speed of 630 m/s. The calculation uses the known Stark shift of metastable CO [32] and the electric fields obtained from SIMION [47]. The trajectories of, typically, 5×10^5 molecules with random initial positions and velocities are traced through a 96-lens array by numerical integration. Line (i) shows the acceptance obtained for a set of perfect linear lenses with $E_0 = 95$ kV/cm, $a_3/a_1 = 1/7$ and $r_0 = 1$ mm. The lens aperture, d , is taken to be 2.1 mm for reasons that will become clear shortly. Since this line is for perfect lenses, it sets the scale for the forthcoming cases. Line (ii) shows the acceptance obtained when the force has a small non-linearity, corresponding to the real field of the four lens geometry of Fig. 3(a), with the two high voltage electrodes held at ± 10 kV and the other two grounded. Once again, r_0 is 1 mm and this gives $E_0 = 95$ kV/cm. End-effects are not considered. The curve displays structure that is absent in the ideal case, and the region of high acceptance is seen to be narrower. We chose the value of d in the ideal case (curve (i)) so as to give the same maximum acceptance. This suggests the definition of an effective aperture, d_{eff} , 2.1 mm in this case. It is interesting to

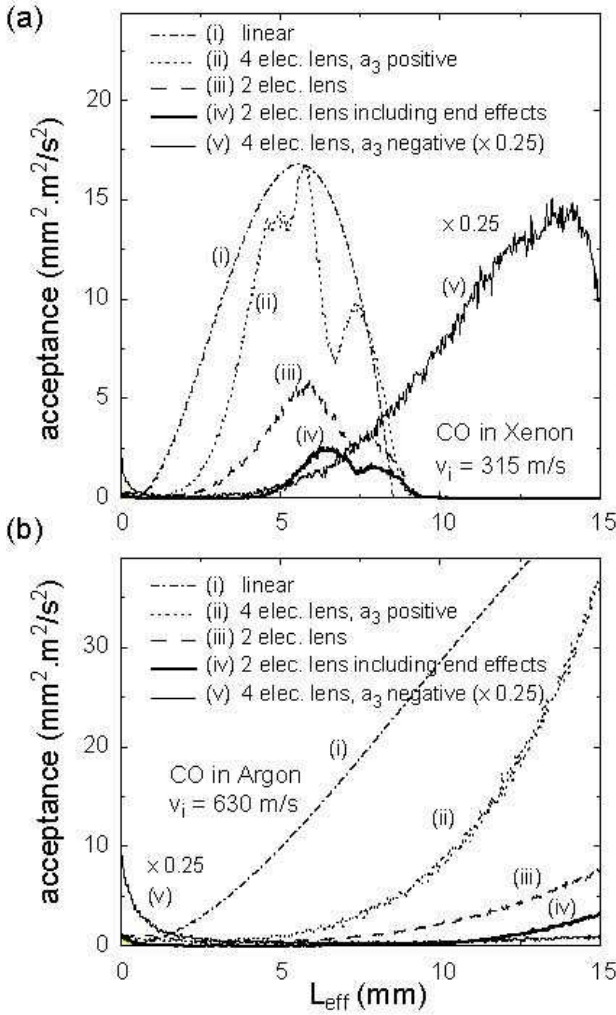


FIG. 8: The acceptance along the solid lines indicated in Fig. 7 for (a) CO seeded in Xenon ($v_z=315$ m/s) and (b) CO seeded in Argon ($v_z=630$ m/s). Lenses with four different electrode geometries have been used, as indicated in the legend. For comparison, the transmission of perfectly linear lenses with a minimum aperture of 2.1 mm is also shown.

note that this effective aperture is slightly larger than the real 2 mm gap between the two electrodes at high voltage. This occurs because the beam envelope is smaller in the defocusing direction than in the focusing direction, and the smaller gap is in the defocusing direction. The 2D transverse acceptance scales as d_{eff}^4 . We next increase the size of the non-linear contributions to the force, by removing the two grounded electrodes of Fig. 3(a). As discussed in Sec. IV, this approximately doubles the ratio a_5/a_3 . All other parameters are kept constant, and end-effects are not yet considered. The acceptance in this case is given by line (iii). We find the impact of the non-linearities to be very detrimental indeed. The effective aperture is reduced to 1.6 mm. As shown by line (iv), a further reduction in acceptance occurs when we introduce the fringe-field aberrations at the entrance and exit

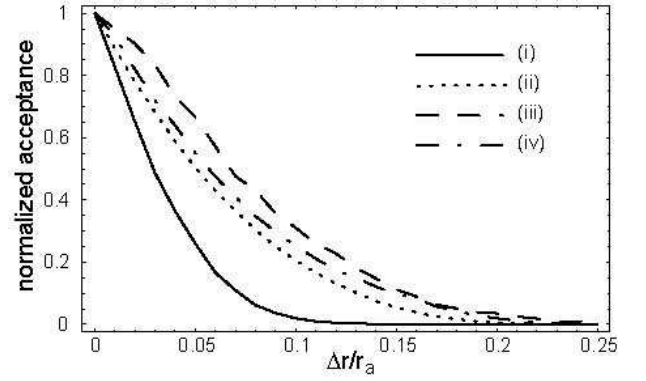


FIG. 9: The calculated acceptance for an array of 96 ideal lenses, as a function of the degree of misalignment (defined in the text). Random (i) and constant (ii) misalignments of a $FODO$ array with $\kappa=50$ m $^{-1}$, $L=S=15$ mm. Random (iii) and constant (iv) misalignments of a $(FO)^3(DO)^3$ array with $\kappa=38.7$ m $^{-1}$, $L=6$ mm and $S=24$ mm.

of each lens. Here, the electrodes of the two-rod lens have hemispherical ends of radius 3 mm as outlined in Sec. IV B. The effective aperture for this case is 1.3 mm. We have also considered the four-electrode geometry of Fig. 3(b), with the electrodes at ± 10 kV and $r_0 = 1$ mm, giving $E_0 = 47$ kV/cm. As discussed in Sec. IV, this geometry results in very small non-linearities, the ratio a_5/a_3 being a factor of 10 smaller than in the two-rod case. The calculated acceptance is shown by line (v) and is divided by a factor 4 for ease of comparison. As E_0 , and hence Ω is smaller in this case, the maximum acceptance is shifted to higher values of L . The effective aperture for this configuration is 2.9 mm making it by far the most effective configuration considered. Note that this effectiveness is due to the small value of a_5/a_3 and not due to the sign of a_5/a_3 ; indeed, calculations show that if we reverse the sign the acceptance is the same. As mentioned in Sec. IV, a disadvantage of this geometry is that the field on axis is only half that of the two-rod geometry, for the same maximum electric field. A decelerator composed of these 4-rod lenses would therefore require twice as many deceleration stages as one composed of 2-rod lenses. The much improved acceptance comes at the cost of increased decelerator length.

Finally in this section, we discuss how the inevitable misalignments of a real machine affect the transverse acceptance. We consider two types of misalignment. In the first type, referred to as ‘random’, the centre of each lens is displaced horizontally and vertically from the axis by amounts chosen at random from normal distributions with full-width at half-maximum Δr . In the second type, referred to as ‘constant’, lenses that focus in the horizontal direction are perfectly aligned to one another and define the axis, while the lenses that focus in the vertical direction are all displaced from the axis by an amount Δr in both transverse directions. These types of mis-

alignment tend to occur naturally in the construction of the decelerator. For example, in our decelerators, each electrode is mounted into one of four common bars to which the high voltages are applied. The degree of random misalignment is determined by the machining precision and the construction technique. Misalignment of the four bars relative to each other results in a constant displacement of the horizontal lenses from the vertical lenses.

We have calculated how the transverse acceptance of the decelerator diminishes as the degree of misalignment increases. Sensitivity to misalignments is found to depend somewhat on the values of κ , L and S . Some representative cases are shown in Fig. 9. This figure gives the 2D transverse acceptance for an alternating gradient array of 96 ideal lenses (linear force, no end effects) as a function of the degree of misalignment, $\Delta r/r_a$, r_a being the radius of the circular aperture defined by the lenses. Each line in the figure has been normalized to the acceptance obtained for perfect alignment. Line (i) gives the result in the case of random misalignments in a *FODO* array with $\kappa=50\text{ m}^{-1}$, $L=15\text{ mm}$ and $S=15\text{ mm}$. One sees that random misalignments of $\Delta r \sim 0.03r_a$ are sufficient to reduce the acceptance by 50%. Line (ii) plots the effect of a constant misalignment for the same parameters, showing this to be a less severe misalignment in this case. A 50% drop in acceptance is reached when this misalignment reaches $\Delta r \sim 0.05r_a$. Lines (iii) and (iv) plot the random and constant cases for a $(FO)^3(DO)^3$ array with $\kappa=38.7\text{ m}^{-1}$, $L=6\text{ mm}$ and $S=24\text{ mm}$. Here, the acceptance is not so sensitive to the random misalignments, while the sensitivity to the constant misalignment is the same as for the *FODO* case. These curves give some typical scenarios. In general, we find that the transmission is less sensitive to misalignments for smaller values of κL , and that misalignments are most severe when the array is operated close to the stability boundary at $\Phi = \pi$.

In our decelerators with $r_a=1\text{ mm}$, we have achieved values of approximately $20\text{ }\mu\text{m}$ for the size of the random misalignment by specifying tight machining tolerances where appropriate. An alignment jig was used to reduce the constant type of misalignment below $\sim 50\text{ }\mu\text{m}$.

B. Longitudinal motion

In order to decelerate or accelerate the molecules, time-varying electric fields are applied. A molecule in a high-field seeking state will gain kinetic energy as it enters the field of a lens, while it loses kinetic energy as it leaves the lens, as shown schematically in Fig. 1(b). If the electric field is switched on while the molecule is inside a lens there is no change to its kinetic energy but the molecule will decelerate as it leaves the lens. The moment when the field is switched on determines the effective length L_{eff} of the lens and hence the focusing properties. The moment when the field is switched off determines the deceleration properties of the lens. We switch off the

electric fields when the molecules have not yet left the field of a lens completely, as shown in Fig. 1(b). This ensures that molecules at the head of the pulse lose more kinetic energy, while those at the tail lose less. In this way, molecules with a suitably narrow spread of longitudinal position and velocity can be confined to a small area of phase-space throughout the decelerator. This behaviour, known as phase stability, has been discussed extensively in the context of decelerating weak-field seeking molecules [48].

To analyze the longitudinal motion, we begin by Taylor expanding the on-axis potential energy of a single deceleration stage (see Fig. 10) around the point of inflection at $z = 0$:

$$W(z) = W(0) + W'(0)z + W'''(0)z^3 + \dots, \quad (20)$$

where $W'(0) = \left. \frac{\partial W}{\partial z} \right|_{z=0}$, $W'''(0) = \left. \frac{\partial^3 W}{\partial z^3} \right|_{z=0}$ and we have used the fact that $\partial^2 W / \partial z^2|_{z=0} = 0$. Close to $z = 0$ the potential energy can be approximated using the first two terms only. The switching sequence is constructed such that a hypothetical molecule, the so-called ‘synchronous molecule’, always reaches the same position z_s of the relevant lens at the moment when the fields are turned off. The change in kinetic energy of the synchronous molecule is the same in every lens, $W_{\text{lens}} - W(z_s)$, W_{lens} being the Stark shift of the molecule inside the lens.

When the energy taken out per stage is small compared to the total kinetic energy of the molecules [48], i.e., when $\Delta v \ll v$, one can describe this change in energy as originating from a constant force

$$F_s = \frac{W_{\text{lens}} - W(z_s)}{(L + S)}, \quad (21)$$

where $(L + S)$ is the distance that the synchronous molecules travels between two subsequent switching times. The difference of the force on a non-synchronous molecule at position z and the force on the synchronous molecule at position z_s is now given by

$$F - F_s = \frac{-W(z) + W(z_s)}{(L + S)} \approx -\frac{W'}{(L + S)}(z - z_s). \quad (22)$$

Consequently, the non-synchronous molecules oscillates around the synchronous molecule with an angular frequency given by

$$\omega_z = \sqrt{\frac{W'}{m(L + S)}}, \quad (23)$$

with m being the mass of the molecules.

In our experiment with metastable CO molecules, described in Sec. VI, $L + S=30\text{ mm}$, and

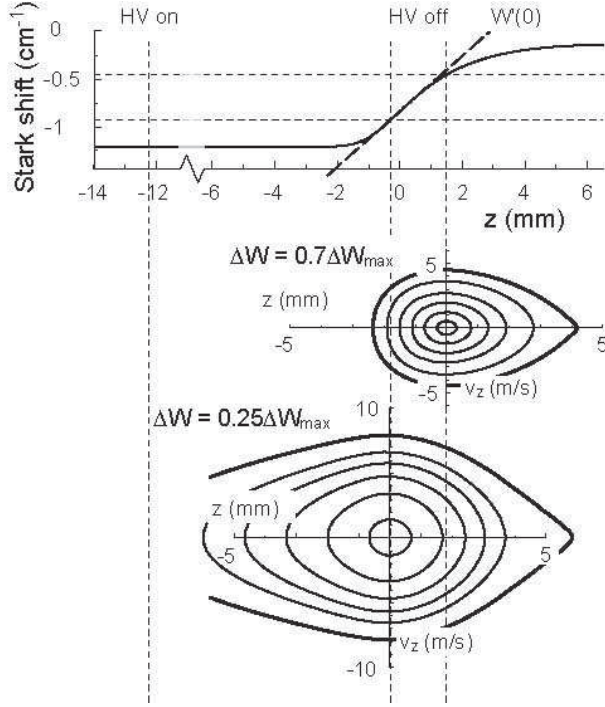


FIG. 10: The Stark shift of metastable CO ($a^3\Pi_1$, $v'=0$, $J'=1$, $M\Omega=1$) molecules as a function of their position along the molecular beam axis. The dotted lines indicate the position of the synchronous molecule when the electric fields are switched on and off for two different settings of the decelerator (expressed as the energy change per stage, ΔW , compared to the maximum possible energy change, ΔW_{max}). In the lower part of the figure some (closed) trajectories in phase-space are shown for non-synchronous molecules, relative to the position and velocity of the synchronous molecule.

$W'(0)=0.29\text{ cm}^{-1}/\text{mm}$ resulting in a longitudinal frequency $\omega_z/2\pi=320\text{ Hz}$.

Figure 10 shows the trajectories of a few non-synchronous molecules, plotted in phase space relative to the position and velocity of the synchronous molecule. From these numerical simulations, non synchronous molecules are found to oscillate around the synchronous molecule with a frequency of $\omega_z/2\pi=330\text{ Hz}$, close to the frequency given by Eq. (23). The thick curves in Fig. 10 show the outermost trajectories of molecules that are still phase stably decelerated. The longitudinal acceptance is about $50\text{ mm}\cdot\text{m/s}$, when $\Delta W = 0.7\Delta W_{max}$, and three times larger when $\Delta W = 0.25\Delta W_{max}$.

Alternating gradient deceleration can also be applied to low-field seeking molecules. In this case, a slightly more complicated switching pattern must be used to achieve both longitudinal and transverse stability. Suppose we want the synchronous molecule to lose an energy $0.5\Delta W_{max}$ per stage. The fields should be turned on well before the synchronous molecule approaches the lens, and turned off again when it is half way up the potential hill. This ensures that non-synchronous molecules

oscillate around the synchronous one as before. Once the molecules are well inside the lens, the fields are turned on again to focus the molecules, and must be turned off before they approach the exit to ensure that they are not accelerated out of the lens. The first high voltage pulse determines the amount of deceleration whilst the second determines the effective length of the lens.

C. Coupling between the longitudinal and transverse motion

The transverse stability depends on the longitudinal velocity because κ is inversely proportional to v_z . Suppose the experimental settings at the start of the decelerator correspond to the point $(\kappa L, \kappa S)$ indicated by the dot in the transverse acceptance plot of Fig. 7. As the molecules are decelerated, their position on this plot moves away from the origin along the dashed line. Eventually, this point will move out of the region of stability, and the beam will be lost. To avoid this, either Ω or L and S must be altered along the array in sympathy with the decreasing speed. A decrease in Ω could be achieved by decreasing the curvature of the electric field. This could be done without altering the on-axis field, which governs the energy loss per stage. However, the transverse acceptance is proportional to Ω , and unless the decrease in Ω is compensated by an increase in d , this will lead to beam loss. A more satisfactory approach is to decrease L and S so that L/v_z and S/v_z remain constant. With this approach the lenses will be long at the beginning of the decelerator and since deceleration occurs only at the end of each lens the overall length may then become undesirably large. That problem can be circumvented by splitting each lens into several parts, i.e., by replacing the $FODO$ array with the more general $(FO)^n(DO)^n$ array. As the velocity is decreased, n is also decreased until, at the end of the decelerator, $n = 1$. In this way the beam can be decelerated stably to a small fraction of its initial speed.

In the longitudinal direction, molecules oscillate around the position of the synchronous molecule, causing the effective lens length experienced by a molecule to vary according to the phase of its longitudinal oscillation. This also couples the longitudinal and transverse motions, possibly leading to parametric amplification of the transverse oscillation [49]. The coupling can be suppressed by designing the lenses to be long compared to the longitudinal spread of the decelerated beam.

VI. 2D IMAGING OF AN AG DECELERATED BEAM OF CO MOLECULES

In order to demonstrate the performance of the alternating gradient decelerator, we have carried out experiments on CO molecules in the $a^3\Pi$ state. The main reason for choosing metastable CO molecules for these

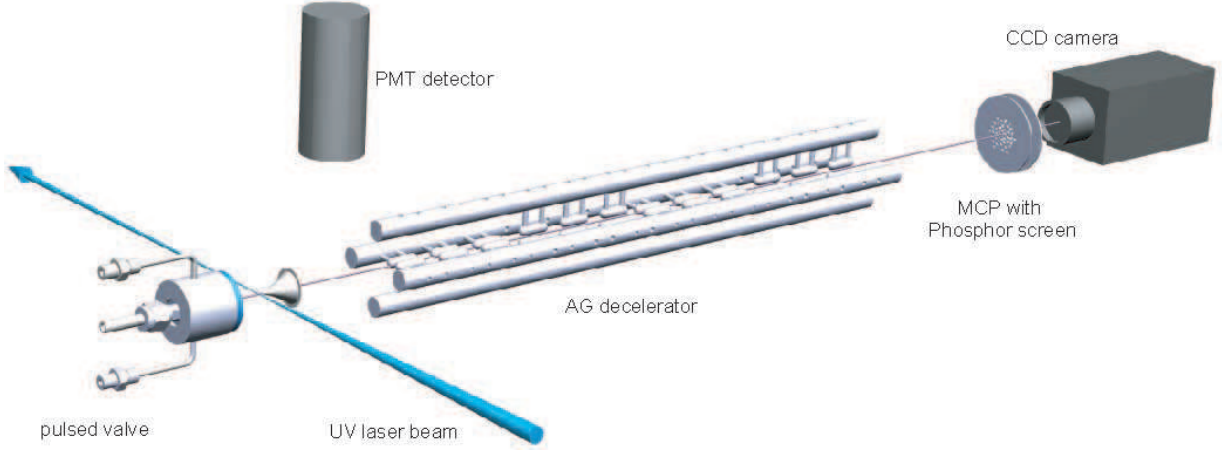


FIG. 11: Scheme of the experimental setup. CO molecules are prepared by UV laser excitation to a high-field seeking level of the metastable $a^3\Pi$ state and pass through an array of 12 lenses arranged in the $(FO)^3(DO)^3$ configuration, with the last group of electrodes oriented vertically. The transverse distribution of high-field seeking metastable CO molecules is recorded 20 cm after the decelerator using a micro channel plate, phosphor screen and CCD camera.

experiments is that (i) they can be prepared in a single quantum state at a well-defined position and time, and (ii) their velocity distribution as well as their transverse distribution can be readily recorded. A scheme of the experimental setup is shown in Fig. 11. A pulsed beam of CO is produced by expanding a mixture of CO with either Xe or Ar into vacuum, using a modified solenoid valve. When seeded in Argon the mean velocity of the beam is $v_i=630$ m/s, corresponding to an initial CO kinetic energy of $E_{kin} = 480$ cm $^{-1}$. When Xenon is used and when the valve housing is cooled to 180 K (just above the boiling point of Xe at the pressure used) the mean velocity of the CO molecules in the beam is reduced to 315 m/s (mixture of 20% CO in Xe) or to 275 m/s (mixture of 5% CO in Xe) corresponding to initial kinetic energies of 120 cm $^{-1}$ and 89 cm $^{-1}$, respectively. In all cases, the velocity spread is approximately 10%, corresponding to a translational temperature of about 1 K.

The metastable CO molecules are prepared in a single quantum state by direct laser excitation on the spin-forbidden $a^3\Pi$ ($v'=0$) \leftarrow $X^1\Sigma^+$ ($v''=0$) transition, using narrow-band pulsed 206 nm (6.0 eV) radiation. In the experiments reported here, the laser is tuned to excite the lower Λ -doublet component of the $J'=1$ $a^3\Pi_1$ level via the $R_2(0)$ transition. By setting the polarization of the laser perpendicular to the stray electric fields present in the excitation region only the $M\Omega = 1$ high-field seeking level is prepared.

The CO molecules pass through a 1.0 mm diameter skimmer into a second, differentially pumped, vacuum chamber housing the 35 cm long AG decelerator. The decelerator consists of 12 equidistant 20 mm long lenses, separated by 10 mm long drift regions. The lenses are arranged in four groups of three, with the first group of electrodes oriented horizontally and the

last group of electrodes oriented vertically. The lenses are formed from two circular electrodes (bold white lines of Fig. 3(a)), with $r_0=1$ mm and $R=3$ mm, and have hemispherical ends. The two opposing rods are simultaneously switched between 0 kV and ± 10 kV by two independent high voltage switches. The electric field on the axis is 95 kV/cm, corresponding to a Stark shift of -1.2 cm $^{-1}$ for the metastable CO molecules. The Stark shift on the molecular beam axis is shown as a function of z in Fig. 1(b).

The molecules land on a micro-channel plate (MCP) detector placed on the beam axis. The 6 eV energy of the excited state is sufficient to release Auger electrons from the surface. These are amplified and detected on a phosphor screen using a CCD camera (LaVision GmbH). Thus, the 2D distribution of the metastable CO beam is recorded. The detection efficiency of the MCP detector is estimated to be about 10^{-3} [50]. Detection efficiencies $> 10\%$ can be obtained by letting the molecules impinge on a flat gold surface kept at 500 K and redirecting the Auger electrons towards an MCP mounted off-axis. Unfortunately, our attempts to build sufficiently distortion-free optics to image the electrons from the gold surface onto the MCP detector failed. Therefore, the longitudinal characteristics of the decelerator are recorded using the gold plate detector, but the 2D distribution of the decelerated CO is measured with the MCP directly intercepting the beam. The initial intensity of the metastable CO beam is monitored simultaneously by detecting the $a^3\Pi \leftarrow X^1\Sigma^+$ fluorescence near the entrance of the AG decelerator with a photomultiplier tube (PMT).

Figure 12 shows the measured time-of-flight (TOF) distributions for several values of the energy change per stage, ΔW . The timing sequences were chosen so that the decelerator would always act on a group of molecules

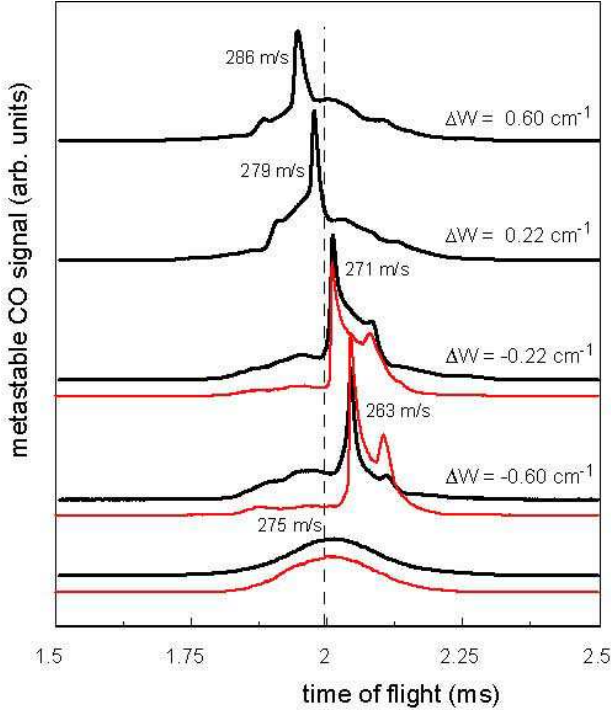


FIG. 12: Observed time-of-flight (TOF) distributions of metastable CO molecules over the 54 cm path length through the apparatus, for 4 different settings of the decelerator (expressed as the energy change per stage, ΔW). The lowest curve shows the TOF-distribution when the electric fields are off. The measurements (thick curves) have been given an offset for clarity. The thin curves show the results of 3D trajectory calculations. The vertical dashed line indicates the expected arrival time of a molecule flying with a constant velocity of 275 m/s.

with initial speeds centred on $v_i = 275$ m/s. The lowest curve is the TOF distribution obtained with no voltages applied to the decelerator. Molecules with a speed of 275 m/s arrive at the time indicated by the dashed line in the figure. Using the 12 stages, the speed can be reduced to 263 m/s, or increased to 286 m/s, depending on the timing of the switched fields. In these experiments the decelerator was operated at ± 8 kV. The thin curves showing the results of the trajectory calculations discussed earlier describe the TOF distributions for the decelerated bunch rather well. Similarly good agreement is obtained in the simulation of the accelerated beam (not shown). The ratio of the time-integrated signal with decelerator on and off is ~ 1.5 as also predicted by our simulations. This ratio is about 10 times larger than measured in a previous experiment on metastable CO [11].

Figure 13 shows transverse distributions of the molecules, measured 20 cm downstream from the decelerator exit for a variety of effective lens lengths. The imaging detector is switched on for a short period (20 μ s when $v_i = 630$ m/s and 40 μ s when $v_i = 315$ m/s) so that only the decelerated molecules are detected. The images

are formed from $\sim 10^4$ detected molecules accumulated over many shots (2000 when $v_i = 630$ m/s and 10^4 when $v_i = 315$ m/s). The false colour is a measure of the number of molecules detected in each pixel. A calculated spatial distribution is shown beside each experimental image.

We discuss first the data with $v_i = 630$ m/s, Fig. 13(a). The top image shows the 2D distribution obtained when there are no voltages on the decelerator. As expected, this measurement simply shows equally distributed molecules within the aperture formed by the electrodes. The detected distribution has a width-to-height ratio of about 1.3 because the last 3 electrode pairs are oriented vertically and end 9 cm closer to the detector than the last horizontal electrode pairs. By looking at the outline of the electrodes, one can also see that the lens array was not perfectly aligned. Indeed, the centre of the horizontal lens set is displaced by 250 μ m from the center of the vertical set (we have since reduced this misalignment to less than 50 μ m). This misalignment has been included in the simulations.

The remaining images in Fig. 13(a) show how the profile of the beam changes as the effective length of the lenses is increased. We consider the vertical direction first. In this direction, the last set of lenses are defocussing, and the beam is diverging when it exits the decelerator. One might expect this divergence to increase with increasing lens length. However, the smaller size of the beam inside the defocussing lenses (compare (a) and (b) in Fig. 6) tends to compensate for the increased power of those lenses. As a result, the vertical divergence changes very little in our experiments and the height of the distribution is approximately constant in all the images. In the horizontal direction, the last set of lenses are focussing lenses, and so the beam is converging when it exits the decelerator. In contrast to the defocussing lenses, the size of the beam inside the focussing lenses is fixed, being determined by the lens aperture. As the lens length increases the exiting beam converges more strongly and so the width of the detected distribution decreases. When the lens length is about 8 mm, a focus is formed in the plane of the detector. Here, the settings correspond to the dot placed on the transverse acceptance plot of Fig. 7(b), where the phase-advance is $\pi/6$. The focus that is formed is rather aberrant, resembling a cross rather than a vertical line. As we will see shortly, the aberration is caused by non-linearities in the transverse forces. When the length is increased beyond 8 mm the focus lies in frontupstream of the detector and the horizontal width begins to increase again. In all cases, the experimental images agree very well indeed with the simulations.

Turning now to the data with $v_i = 315$ m/s (Fig. 13(b)), we see that the lower forward speed results in the focus being formed in the plane of the detector for a smaller value of L_{eff} . Using a thin lens approximation, the focal length is $1/\kappa^2 L$. Since halving v_i , doubles κ we expect the focus to be formed for $L_{eff} = 2$ mm, exactly as observed in the data. These settings correspond to the

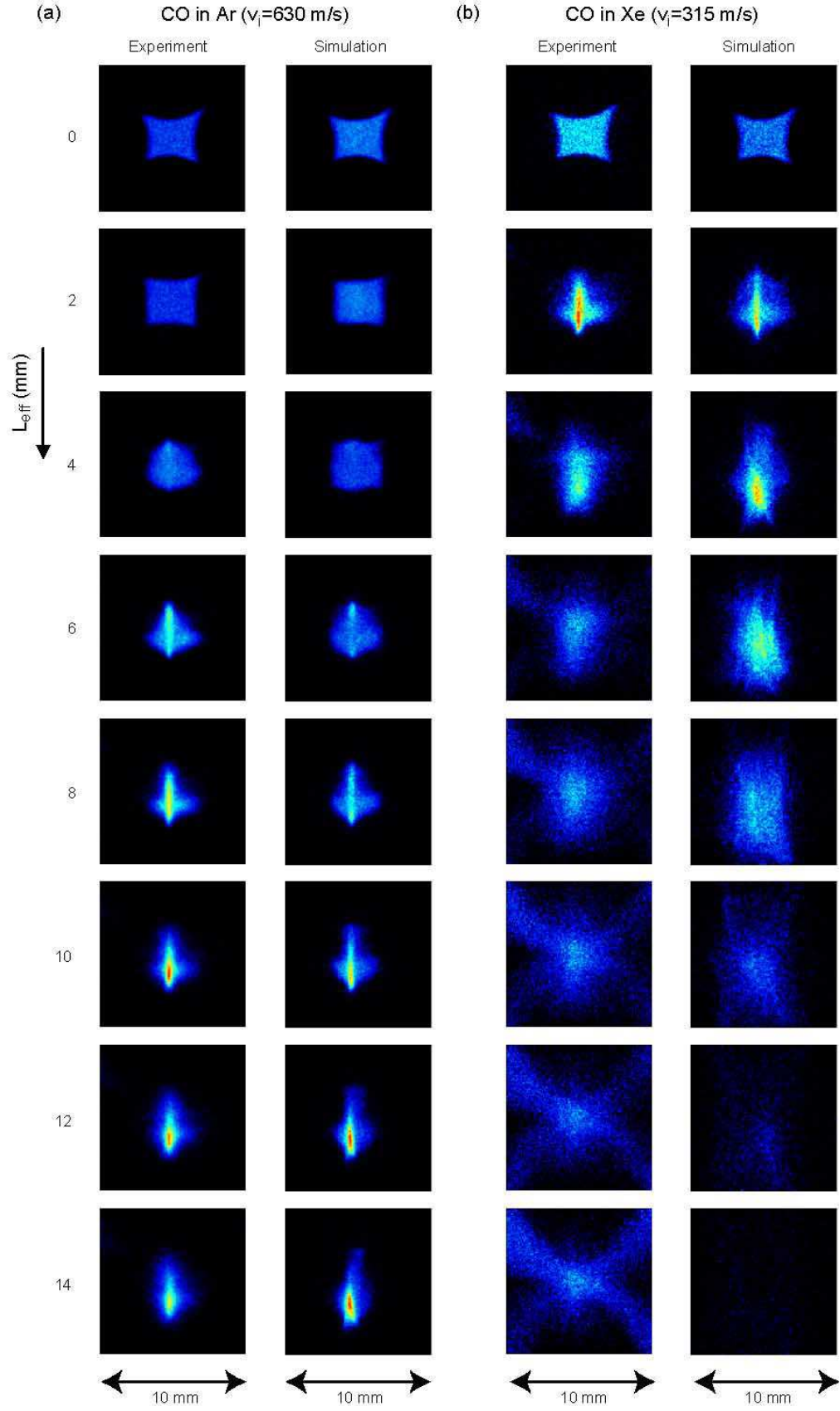


FIG. 13: Observed and calculated 2D distributions of a decelerated beam of CO molecules with an initial speed of (a) 630 m/s and (b) 315 m/s, for various values of the effective lens length (in mm).

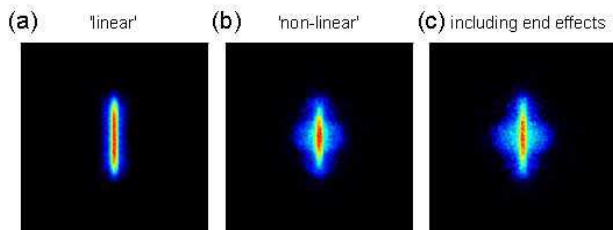


FIG. 14: Simulated 2D distributions 20 cm downstream from the decelerator exit, for CO molecules with $v_i = 630$ m/s. (a) Linear force, (b) true force, excluding end effects, and (c) true force.

cross placed on Fig. 7(b), where again, the phase advance is $\pi/6$. As L_{eff} is increased beyond 2 mm, the horizontal focus lies progressively further in front of the detector and so the detected distribution grows progressively wider. When $L_{eff} > 10$ mm, the trajectories become unstable and there is a very sudden drop in the intensity of the simulated data. The experimental images show a less rapid drop in intensity, CO molecules being observed near the molecular beam axis, even when $L_{eff} = 14$ mm. In addition, a diagonal cross shape is observed in the experimental data. This we attribute to molecules so strongly focused in the first three lenses that they escape and subsequently fly outside the decelerator. Our simulation could not follow such trajectories because the field used was bounded 4 mm from the beam axis and molecules outside this area were considered lost. We surmise that these molecules also give rise to the intensity observed at the centre of the images.

By integrating the intensity of the measured distributions one obtains the acceptance as a function of the effective length of the lenses, analogous to the calculations shown in Fig. 8. However, a frequency drift of the UV excitation laser during the measurements compounded by the rather low counting rates, resulted in integrated beam fluctuations of more than 50%, preventing a clear comparison of measured and calculated acceptances.

Figure 14 reveals the origin of the aberrations present at the focus. We repeated the calculation for the case of $v_i = 630$ m/s, $L_{eff} = 8$ mm. In (a), the calculation was performed assuming a perfectly linear force, and we find the focus to be a vertical line without aberration. The aberrations appear when we include the non-linearities in the force (Fig. 14(b)), showing this to be the primary factor in degrading the image quality. The addition of the end-effects degrades the image quality a little further, as shown in (c).

VII. SUMMARY AND CONCLUSIONS

In this paper we have presented the principles of alternating gradient deceleration of polar molecules along with the criteria that govern decelerator design and op-

eration. We began by showing that heavy molecules in low-lying rotational states seek strong field, and so cannot be confined by static electric fields. Alternating gradient focusing can be used to stabilize the trajectories of such molecules in a Stark decelerator. We showed how the electric fields required to achieve alternating gradient focusing can be produced using simple electrode geometries. The simplest of these, the two-rod geometry shown in Fig. 3(a), has already been used to decelerate metastable CO and YbF molecules [11, 12], and was used in the imaging experiments presented here. This electrode geometry gives rise to significant non-linear terms in the force. These can be reduced, without reducing the on-axis field, by the addition of a pair of grounded electrodes. The non-linearities are further reduced when four high voltage electrodes are arranged as in Fig. 3(b), but at the cost of reducing the field on the axis. The fringe-fields of the lenses, essential for deceleration, tend to increase the defocusing power relative to the focusing power near the entrance and exit of the lens. This detrimental effect can be reduced by terminating the rods more gradually. The four-rod geometries are also more favourable than the two-rod geometry in this respect.

We discussed the motion of the molecules through the decelerator in detail. When the transverse forces are perfectly linear, the transverse motion is best described using the formalism first set out in the context of the alternating gradient synchrotron [19], and outlined in Sec. V A. The trajectories are described in terms of the phase-advance and the envelope function. The transverse phase-space distribution is an ellipse whose shape evolves periodically through the lattice, but whose area is a constant. Figure 6 illustrates the evolution of the beam envelope and the phase-space ellipse. We calculated the transverse acceptance of an array of ideal lenses as a function of κL and κS (Fig. 7) and found the maximum acceptance to be $0.186d^2\Omega$, where d is the transverse aperture and Ω given in terms of the mass, the effective dipole moment and the electric field curvature by Eq. (12). Non-linearities in the transverse forces, and the fringe-fields of the lenses, severely reduce the transverse acceptance (Fig. 8). Furthermore the degree of lens-to-lens alignment required to achieve a high transmission was found to be demanding but attainable with high-precision machining.

The longitudinal motion was discussed in terms of a simple model of phase-stability. The most significant coupling between transverse and longitudinal motion is that the transverse motion depends on the forward speed. As the speed is reduced the molecules spend more time in each lens. A good way to handle this is to use an $(FO)^n(DO)^n$ structure with n larger at the entrance than at the exit of the decelerator.

We studied the focusing properties of an alternating gradient decelerator experimentally using an array of 12 lenses, by measuring 2D images of a decelerated beam of metastable CO molecules. Trajectory simulations of this experiment reproduce the experimental findings. Non-

linearities in the force and effects due to rounded ends of the electrodes need to be included to obtain close agreement. These experimentally verified simulations predict a transverse acceptance of 2 (mm.m/s)^2 , see Fig. 8, and a longitudinal acceptance of 50 mm.m/s , see Fig. 10. These numbers can be compared to those that have been presented earlier for light molecules in low-field seeking states. In the Stark deceleration of ammonia, for instance, a transverse acceptance of 160 (mm.m/s)^2 and a longitudinal acceptance of 10 mm.m/s has been obtained [3]. As discussed above, the transverse acceptance is very much smaller than for ideal lenses and we can expect a more sophisticated lens design to yield a tenfold improvement. A further increase of the acceptance could be achieved by increasing the transverse aperture, although a corresponding increase in the applied voltages would be needed in order to maintain the same on-axis electric field.

In discussing the alternating gradient decelerator, we have also laid out the principles of a guide for high-field-seeking molecules. Unlike a decelerator, a guide does not need to be divided into segments along the beamline, and so can be free of end-effects. The symmetric four electrode geometry of Fig. 3(b) makes an ideal guide because its aberrations are small, its acceptance is high, and the focus and defocus directions are very easily switched. Another interesting application is to use this geometry as an m/μ_{eff} filter, the equivalent of an m/q filter for ions [46]. The resolution of such a filter can be increased, at the expense of the acceptance, by tuning the focus-defocus duty-cycle away from 50%. In one plane, the de-

focusing lenses are then longer than the focusing lenses making the stability region narrower and so increasing the resolution. Calculations indicate that a resolution $\Delta(m/\mu_{\text{eff}})/(m/\mu_{\text{eff}}) \sim 0.1$ can be obtained at the cost of a factor of 4 in acceptance relative to the maximum.

The decrease in velocity achieved in an AG decelerator so far has been rather small, but since the trajectories of the molecules through the decelerator are inherently stable, no additional losses are expected when the number of stages is further increased. For the molecules listed in Table I, and for many others, approximately 100 electric field stages are sufficient to bring them to rest. These molecules could subsequently be stored in a storage ring [51] or in an AC-trap [52].

VIII. ACKNOWLEDGEMENTS

We acknowledge the expert technical assistance of H. Haak and J. Dyne. We thank B. Friedrich and J. van Veldhoven for helpful discussions and S.Y.T. van de Meerakker and F. Filsinger for help with performing the calculations of the Stark effect. This work was supported by the ‘Cold Molecules’ network of the European Commission and, in the UK, by EPSRC and PPARC. H.L.B. acknowledges financial support from the Netherlands Organisation for Scientific Research (NWO) via a VENI-grant. M.R.T. and E.A.H. acknowledge the support of the Royal Society.

-
- [1] J. Doyle, B. Friedrich, R.V. Krems, and F. Masnou-Seeuws, *Eur. Phys. J. D* **31**, 1 (2004), and references therein.
 - [2] H.L. Bethlem, G. Berden, and G. Meijer, *Phys. Rev. Lett.* **83**, 1558 (1999).
 - [3] H.L. Bethlem, F.M.H. Crompvoets, R.T. Jongma, S.Y.T. van de Meerakker, and G. Meijer, *Phys. Rev. A* **65**, 053416 (2002).
 - [4] J.R. Bochinski, E.R. Hudson, H.J. Lewandowski, G. Meijer, and J. Ye, *Phys. Rev. Lett.* **91**, 243001 (2003).
 - [5] S.Y.T. van de Meerakker, P.H.M. Smeets, N. Vanhaecke, R.T. Jongma, and G. Meijer, *Phys. Rev. Lett.* **94**, 023004 (2005).
 - [6] S.Y.T. van de Meerakker, I. Labazan, S. Hoekstra, J. Küpper, and G. Meijer, *arXiv:physics/0512194* (2005).
 - [7] E.R. Hudson, C.T. Ticknor, B.C. Sawyer, C.A. Taatjes, H.J. Lewandowski, J.R. Bochinski, J.L. Bohn, and J. Ye, *arXiv:physics/0508120* (2005).
 - [8] S. Jung, E. Tiemann, and C. Lisdat, submitted.
 - [9] J.J. Hudson, B.E. Sauer, M.R. Tarbutt and E.A. Hinds, *Phys. Rev. Lett.* **89**, 023003 (2002).
 - [10] J.J. Hudson, P.C. Condylis, H.T. Ashworth, M.R. Tarbutt, B.E. Sauer and E.A. Hinds, in *Laser Spectroscopy 17*, Edited by E.A. Hinds, A. Ferguson and E. Riis, p. 219 (World Scientific, Singapore, 2005).
 - [11] H.L. Bethlem, A.J.A. van Roij, R.T. Jongma, and G. Meijer, *Phys. Rev. Lett.* **88**, 133003 (2002).
 - [12] M.R. Tarbutt, H.L. Bethlem, J.J. Hudson, V.L. Ryabov, V.A. Ryzhov, B.E. Sauer, G. Meijer, and E.A. Hinds, *Phys. Rev. Lett.* **92**, 173002 (2004).
 - [13] D. Auerbach, E.E.A. Bromberg, and L. Wharton, *J. Chem. Phys.* **45**, 2160 (1966).
 - [14] J.J. Livingood, *Principles of cyclic particle accelerators*. D. van Nostrand, Inc., New Jersey (1961).
 - [15] J.C. Helmer, F.B. Jacobus, and P.A. Sturrock, *J. Appl. Phys.* **31**, 458 (1960).
 - [16] K.-R. Chien, P.B. Foreman, K.H. Castleton, and S.G. Kukolich, *Chem. Phys.* **7**, 161 (1974).
 - [17] H.-J. Loesch and B. Scheel, *Phys. Rev. Lett.* **85**, 2709 (2000).
 - [18] E.D. Courant, M.S. Livingstone, and H.S. Snyder, *Phys. Rev.* **88**, 1190 (1952).
 - [19] E.D. Courant and H.S. Snyder, *Ann. Phys.* **3**, 1 (1958).
 - [20] D. Kakati and D.C. Lainé, *Phys. Lett.* **24A**, 676 (1967); **28A**, 786 (1969); *J. Phys. E* **4**, 269 (1971).
 - [21] F. Günther and K. Schügerl, *Z. Phys. Chemie* **NF80**, 155 (1972).
 - [22] A. Lübbert, F. Günther, and K. Schügerl, *Chem. Phys. Lett.* **35**, 210 (1975).
 - [23] A. Lübbert, G. Rotzoll, and F. Günther, *J. Chem. Phys.* **69**, 5174 (1978).
 - [24] E.E.A. Bromberg, Ph.D. thesis, University of Chicago

- 1972.
- [25] H.-R. Noh, K. Shimizu, and F. Shimizu Phys. Rev. A **61**, 041601(R) (2000).
 - [26] J.G. Kalnins, J.M. Amini, and H. Gould, Phys. Rev. A **72**, 043406 (2005).
 - [27] J. Kalnins, G. Lamberton, and H. Gould, Rev. Sci. Instr. **73**, 2557 (2002).
 - [28] M. Peter and M.W.P. Strandberg, J. Chem. Phys. **26**, 1657 (1957).
 - [29] H.-J. Loesch and A. Remscheid, J. Chem. Phys. **93**, 4779 (1990).
 - [30] B. Friedrich and D.R. Herschbach, Z. Phys. D **18**, 153 (1991).
 - [31] J.M. Rost, J. C. Griffin, B. Friedrich and D. R. Herschbach, Phys. Rev. Lett. **68**, 1299 (1992).
 - [32] R.T. Jongma, G. von Helden, G. Berden, G. Meijer, Chem. Phys. Lett. **270**, 304 (1997).
 - [33] B.E. Sauer, J. Wang, and E.A. Hinds, J. Chem. Phys. **105**, 7412 (1996).
 - [34] D.R. Borst, T.M. Korter and D.M. Pratt, Chem. Phys. Lett. **350**, 485 (2001).
 - [35] W. Kong and J. Bulthuis, J. Phys. Chem. A **104**, 1055 (2000).
 - [36] L.A. Kaledin, J.C. Bloch, M.C. McCarthy and R.W. Field, J. Mol. Spectroscopy **197**, 289 (1999).
 - [37] W.J. Childs, L.S. Goodman, U. Nielsen and V. Pfeufer, J. Chem. Phys. **80**, 2283 (1984).
 - [38] D.A. Baugh, D. Young Kim and V.A. Cho, L.C. Pipes, J.C. Pettey and C.D. Fuglesang, Chem. Phys. Lett. **219**, 207 (1994).
 - [39] H. Li, K.J. Franks, R.J. Hanson, and W. Kong, J. Phys. Chem. A **102**, 8084 (1998).
 - [40] I. Compagnon, F.C. Hagemeister, R. Antoine, D. Rayane, M. Broyer, P. Dugourd, R.R. Hudgins and M.F. Jarrold, J. Am. Chem. Soc. **123**, 8440 (2001).
 - [41] T.R. Rizzo, Y.D. Park, L.A. Peteanu, and D.H. Levy, J. Chem. Phys. **84**, 2534 (1986).
 - [42] J. Reuss, in *Atomic and Molecular Beam Methods*, Vol. I, ed. G. Scoles, (Oxford University Press, New York, 1988).
 - [43] This field was also considered by Anderson; R.W. Anderson, Book of abstracts of the International Conference on 'Stereodynamics in Chemical Reactions', Schoorl, The Netherlands 2002.
 - [44] T. Junglen, T. Rieger, S.A. Rangwala, P.W.H. Pinkse and G. Rempe, Phys. Rev. Lett. **92**, 223001 (2004).
 - [45] S.Y. Lee, Accelerator Physics (World Scientific, Singapore), (1999).
 - [46] W. Paul, Rev. Mod. Phys. **62**, 531 (1990).
 - [47] D.A. Dahl, Simion 3D Version 6.0, Idaho National Engineering Laboratory, Idaho Falls (USA), (1995).
 - [48] H.L. Bethlem, G. Berden, A.J.A. van Roij, F.M.H. Crompvoets, and G. Meijer, Phys. Rev. Lett. **84**, 5744 (2000).
 - [49] S.Y.T. van de Meerakker, N. Vanhaecke, H.L. Bethlem, and G. Meijer, Phys. Rev. A **73**, 023401 (2006).
 - [50] R.T. Jongma, Th. Rasing, and G. Meijer, J. Chem. Phys. **102**, 1925 (1995).
 - [51] H. Nishimura, G. Lamberton, J. G. Kalnins, and H. Gould, Eur. J. Phys. D **31**, 359 (2004).
 - [52] J. van Veldhoven, H.L. Bethlem, and G. Meijer, Phys. Rev. Lett. **94**, 083001 (2005).
 - [53] We consider focusing in three directions here. It is possible to create fields that focus molecules in high-field-seeking states in the transverse direction while defocusing them in the longitudinal direction. These fields cannot be used for phase-stable deceleration.
 - [54] The condition $\vec{\nabla} \cdot \vec{F} < 0$, is necessary but not sufficient for stability. For instance, the force may vary in such a way that parametric amplification of the amplitude of the trajectories occurs (see, for instance, [49]).
 - [55] A similar expression can be derived for a quadratic Stark shift [13].